Assessment of the equivalent inclusion method for the numerical homogenization of fibrous composites

Antoine Martin, S. Brisard, Stéphane Deleville, Karam Sab

Assessment of the equivalent inclusion method for the numerical homogenization of fibrous composites

Antoine Martin, Sébastien Brisard, Stéphane Deleville and Karam Sab

This is the accepted version of the following article: “Assessment of the equivalent inclusion method for the numerical homogenization of fibrous composites”, which has been published in final form at https://doi.org/10.1016/j.jcp.2023.111943.

Assessment of the equivalent inclusion method for the numerical homogenization of fibrous composites

A. Martin[a,b], S. Brisard[a,*], S. Deleville[c], K. Sab[a]

[a] *Univ Gustave Eiffel, Ecole des Ponts, CNRS, Navier, F-77454 Marne-la-Vallée, France*
[b] *Spie batignolles génie civil, 30 avenue du Général Gallieni, CS 10192, 92023 Nanterre CEDEX*
[c] *Spie batignolles technologies, 30 avenue du Général Gallieni, CS 10192, 92023 Nanterre CEDEX*

Abstract

For the homogenization of fibre composites, the equivalent inclusion method is proposed as an alternative to costly full-field methods and less accurate mean-field or effective-field approaches. We take advantage of the slenderness of the inhomogeneities to overcome the "curse of dimensionality" that was evidenced previously for this method. The resulting method is shown on a number of examples to be both accurate and computationally efficient. It is also extremely versatile, as it applies to a large variety of physical problems (beyond electric conductivity considered here).

Keywords: Homogenization, Conductivity, Equivalent inclusion method, Lippmann–Schwinger equation, Cylindrical inclusions

1. Introduction

At fixed volume, the collective effect of fibers embedded in a homogeneous matrix often surpasses the collective effect of spherical inclusions, embedded in the same matrix. Fibers are therefore frequently used in composite technology to improve the mechanical [6], thermal [5] or even electromagnetic [17] properties of the surrounding matrix.

For engineering design purposes, *predicting* this collective effect is an essential task. However, this homogenization process (predicting the effective properties of the composite from the properties of its constituents) turns out to be technically challenging for slender fibers.

On the one hand, classical mean-field or effective-field homogenization methods [23, 33, 26, 14] do apply to elongated (spheroidal) inhomogeneities. However, these models fail to account for local orientation correlations that are bound to occur when the volume fraction of fibers becomes higher. This is due to the fact that these models are based on the solution to the problem of Eshelby [11], which disregards direct interactions between inhomogeneities.

On the other hand, full-field simulations of the composite are possible in theory [29, 25, 15]. However, the spatial discretization is governed by the (small) *transverse dimensions* of the inhomogeneities. As a consequence, microstructures are difficult to mesh and the resulting simulation has a very large number of unknowns.

Clearly, there is some space for an intermediate method between mean-field/effective-field and full-field methods, that should be more accurate than mean-field or effective-field methods, while requiring less computational resources than full-field methods. The equivalent inclusion method (referred to as the EIM below) developed by Moschovidis and Mura [24] is shown in this paper to be an attractive contestant in the case of slender (elongated) inhomogeneities. Indeed, based on ideas that are similar to the early work of Eshelby [11], Moschovidis and Mura [24] introduce an approximation of the interactions between inhomogeneities, an ingredient which is lacking in mean-field or effective-field approaches. The cluster method introduced by Molinari and El Mouden [22] is based on essentially the same ideas (see also [10] and [32]). The EIM has been applied by various authors [12, 4, 28, 13, 37], for various types

*Corresponding author
Email address: sebastien.brisard@univ-eiffel.fr (S. Brisard)

of physical settings (such as linear elasticity, thermal conductivity or fluid mechanics). It has also been extended to non-spherical [10] or inhomogeneous [32] inclusions.

Several variants of the method have also been considered [38, 36]. In particular, Brisard et al. [7] introduced a Galerkin-based variational form of the EIM. At that time, *exponential* convergence with respect to the polynomial order was observed. However, for 3D assemblies of spherical inhomogeneities, the number of unknowns becomes impractically high. Since fibers are essentially 1D (rather than 3D) objects, EIM simulations do not necessarily face the same "curse of dimensionality". In this paper, we extend the EIM to slender inhomogeneities. We show how the various influence coefficients can be evaluated. We also show on small systems that the method is remarkably accurate, for a very low computational cost.

It should be noted that the present paper is dedicated to electric conductivity; it readily extends to linear elasticity [7]. In fact, we believe it applies to any type of physical problems where a Green operator (in the sense of Appendix A) can be defined.

This paper is organized as follows. An overview of the EIM is first provided in Sec. 2. The main contribution of this paper is presented in Sec. 3, where slender inhomogeneities are considered. Performance of the resulting method is assessed on one- and two-cylinder systems in Secs. 4 and 5, respectively. It is shown that the discretization must be enriched in the radial direction. Larger systems are considered in Sec. 6. Sec. 7 closes this paper with a few concluding remarks and a discussion of future research directions.

2. Background: the variational form of the EIM

The present section provides an overview of the EIM introduced by Eshelby [11] and Moschovidis and Mura [24] and its variational form [7]. The modified Lippmann–Schwinger equation is introduced in Sec. 2.1. The Galerkin discretization of this equation, leading to the EIM, is presented in Sec. 2.2.

Remark 1. *Brisard et al. [7] have initially formulated the variational form of the EIM within the framework of linear elasticity. Transposition to linear conductivity is straightforward, with the following equivalences: stress ↔ electric flux, strain ↔ electric field, displacement ↔ electric potential.*

2.1. The modified Lippmann–Schwinger equation

Within the framework of electric conductivity, we consider a representative volume element (RVE) Ω of a random heterogeneous material. The conductivity at $\mathbf{x} \in \Omega$ is $\boldsymbol{\sigma}(\mathbf{x})$ (symmetric, positive definite, second-order tensor); $\mathbf{E}(\mathbf{x})$, $\phi(\mathbf{x})$ and $\mathbf{j}(\mathbf{x})$ denote the electric field, the electric potential[1] and the volumic current, respectively, at point $\mathbf{x}$. The apparent conductivity of the RVE Ω, $\boldsymbol{\sigma}^{\mathrm{app}}$, is found from the solution to the following boundary-value problem

$$\Omega : \quad \operatorname{div} \mathbf{j} = 0, \tag{1}$$

$$\Omega : \quad \mathbf{j} = \boldsymbol{\sigma} \cdot \mathbf{E}, \tag{2}$$

$$\Omega : \quad \mathbf{E} = \mathbf{grad}\, \phi, \tag{3}$$

with boundary conditions that are not specified for the time being. Eq. (1) expresses conservation of the electric current; Eq. (2) is Ohm's law; finally, Eq. (3) ensures that the electric field is curl-free.

Classical boundary conditions include [39, 16]: homogeneous current boundary conditions (Neumann), homogeneous electric field boundary conditions (Dirichlet) and periodic boundary conditions. As discussed previously within the framework of linear elasticity [8, 7], these classical boundary conditions must be replaced with *mixed boundary conditions* for the EIM. The RVE Ω is embedded in a homogeneous, infinite matrix with conductivity $\boldsymbol{\sigma}_0$; χ denotes the indicator function of Ω ($\chi(\mathbf{x}) \in \{0, 1\}$ and $\chi(\mathbf{x}) = 1$ iff $\mathbf{x} \in \Omega$). The macroscopic electric field $\overline{\mathbf{E}}$ being prescribed, the mixed boundary conditions are twofold. At infinity, first

$$\|\mathbf{x}\| \to +\infty : \quad \mathbf{E}(\mathbf{x}) \to \overline{\mathbf{E}}, \tag{4}$$

[1] Strictly speaking, $\phi(\mathbf{x})$ is the *opposite* (in the sense of the negative inverse, see https://en.wikipedia.org/wiki/Additive_inverse, last retrieved 2023-01-11) of the electric potential.

then on the boundary $\partial\Omega$ of the RVE

$$\mathbf{x} \in \partial\Omega : \quad [\![\mathbf{j}(\mathbf{x})]\!] \cdot \mathbf{n}(\mathbf{x}) = \bar{\mathbf{j}} \cdot \mathbf{n}(\mathbf{x}), \tag{5}$$

where $\bar{\mathbf{j}} \in \mathbb{R}^3$ is an auxiliary constant, which is found by enforcing that the macroscopic electric field coincides with the prescribed value $\overline{\mathbf{E}}$

$$\langle \mathbf{E} \rangle = \overline{\mathbf{E}}, \tag{6}$$

where angle brackets denote volume averages over the RVE Ω

$$\langle \bullet \rangle = \frac{1}{|\Omega|} \int_\Omega \bullet(\mathbf{x}) \, \mathrm{d}^3\mathbf{x}. \tag{7}$$

As shown previously [8], the motivation for these seemingly complex boundary conditions is the reformulation of problem (1)–(6) as a unique integral equation of the Lippmann–Schwinger type [40]

$$(\boldsymbol{\sigma} - \boldsymbol{\sigma}_0)^{-1} \cdot \boldsymbol{\tau} + \boldsymbol{\Gamma}_0^\infty(\boldsymbol{\tau} - \chi\langle\boldsymbol{\tau}\rangle) = \overline{\mathbf{E}}, \tag{8}$$

where the main unknown is the *polarization* $\boldsymbol{\tau}$

$$\boldsymbol{\tau} = (\boldsymbol{\sigma} - \boldsymbol{\sigma}_0) \cdot \mathbf{E}. \tag{9}$$

In the above modified Lippmann–Schwinger equation, first introduced by Willis [34], $\boldsymbol{\Gamma}_0^\infty$ denotes the Green operator, associated with the conductivity $\boldsymbol{\sigma}_0$ (see definition in Appendix A). It maps the field $\boldsymbol{\tau}$ onto the field $\boldsymbol{\Gamma}_0^\infty(\boldsymbol{\tau})$. For an isotropic reference material ($\boldsymbol{\sigma}_0 = \sigma_0 \, \mathbf{1}$), we have the following expression of the Green operator [9, 31]

$$\boldsymbol{\Gamma}_0^\infty(\boldsymbol{\tau})(\mathbf{x}) = \mathbf{P}_0 \cdot \boldsymbol{\tau}(\mathbf{x}) + \operatorname*{PV}_{\mathbf{x}} \int_{\mathbf{y}\in\Omega} \mathbf{G}_0(\mathbf{y} - \mathbf{x}) \cdot \boldsymbol{\tau}(\mathbf{y}) \, \mathrm{d}^3\mathbf{y}, \quad \text{where} \quad \mathbf{P}_0 = \frac{\mathbf{1}}{3\sigma_0} \quad \text{and} \quad \mathbf{G}_0(\mathbf{r}) = \frac{\mathbf{1} - 3\mathbf{n}\otimes\mathbf{n}}{4\pi\sigma_0 r^3} \tag{10}$$

($r = \|\mathbf{r}\|$ and $\mathbf{n} = \mathbf{r}/r$). In the above equation, "$\mathrm{PV}_\mathbf{x}$" refers to the principal value at $\mathbf{x}$ for spherical excluded regions

$$\operatorname*{PV}_{\mathbf{x}} \int_{\mathbf{y}\in\Omega} f(\mathbf{y}) \, \mathrm{d}^3\mathbf{y} = \lim_{\delta\to 0} \int_{\substack{\mathbf{y}\in\Omega \\ \|\mathbf{y}-\mathbf{x}\|\geq\delta}} f(\mathbf{y}) \, \mathrm{d}^3\mathbf{y} \tag{11}$$

Note that the polarization vanishes at any point $\mathbf{x}$ where $\boldsymbol{\sigma}(\mathbf{x}) = \boldsymbol{\sigma}_0$ [see Eq. (9)]. Therefore, the corrected polarization $(\boldsymbol{\tau} - \chi\langle\boldsymbol{\tau}\rangle)$ is null outside Ω

$$\mathbf{x} \in \mathbb{R}^3 \setminus \Omega : \quad \boldsymbol{\tau}(\mathbf{x}) - \chi(\mathbf{x})\langle\boldsymbol{\tau}\rangle = \mathbf{0} \tag{12}$$

and has null volume average over Ω

$$\langle \tau - \chi\langle\boldsymbol{\tau}\rangle \rangle = \mathbf{0}. \tag{13}$$

From the volume average $\langle\boldsymbol{\tau}\rangle$ of the solution $\boldsymbol{\tau}$ to the modified Lippmann–Schwinger equation (8), the apparent conductivity is readily retrieved. Indeed, using Eq. (9)

$$\boldsymbol{\sigma}^{\mathrm{app}} \cdot \overline{\mathbf{E}} = \langle \boldsymbol{\sigma} \cdot \mathbf{E} \rangle = \langle \boldsymbol{\sigma}_0 \cdot \mathbf{E} + \boldsymbol{\tau} \rangle = \boldsymbol{\sigma}_0 \cdot \langle \mathbf{E} \rangle + \langle \boldsymbol{\tau} \rangle = \boldsymbol{\sigma}_0 \cdot \overline{\mathbf{E}} + \langle \boldsymbol{\tau} \rangle \tag{14}$$

Remark 2. *Note that equivalence between problem* (1)–(6) *and the modified Lippmann–Schwinger equation* (8) *holds for RVEs* Ω *of* ellipsoidal shape *[8].*

Of course, the limit for large RVEs of the apparent conductivity does not depend on the radii of the ellipsoid. In the remainder of this paper, the microstructures under consideration are statistically isotropic. It is therefore natural to use spherical *RVEs.*

2.2. Discretization of the Lippmann–Schwinger equation

We follow a Galerkin procedure to derive an approximate solution to the Lippmann–Schwinger equation (8). Contracting Eq. (8) with a test function $\boldsymbol{\varpi} \in \mathbb{V}$ and volume averaging over Ω delivers the following variational problem

$$\text{Find } \boldsymbol{\tau} \in \mathbb{V} \text{ such that, for all } \boldsymbol{\varpi} \in \mathbb{V}: \quad a(\boldsymbol{\tau}, \boldsymbol{\varpi}) = \overline{\mathbf{E}} \cdot \langle \boldsymbol{\varpi} \rangle \tag{15}$$

where $\mathbb{V}$ is the set of square integrable vector fields supported in Ω [8], and a is the following bilinear form

$$a(\boldsymbol{\tau}, \boldsymbol{\varpi}) = \langle \boldsymbol{\varpi} \cdot (\boldsymbol{\sigma} - \boldsymbol{\sigma}_0)^{-1} \cdot \boldsymbol{\tau} \rangle + \langle \boldsymbol{\varpi} \cdot \boldsymbol{\Gamma}_0^{\infty}(\boldsymbol{\tau} - \chi \langle \boldsymbol{\tau} \rangle) \rangle. \tag{16}$$

Discretization of the above variational problem then follows a standard Galerkin procedure. Introducing the discretization parameter $p \in \mathbb{N}$ (to be defined below) and the finite-dimensional discretization subspace $\mathbb{V}^p$ of $\mathbb{V}$, we consider the following variational problem

$$\text{Find } \boldsymbol{\tau}^p \in \mathbb{V}^p \text{ such that, for all } \boldsymbol{\varpi}^p \in \mathbb{V}^p: \quad a(\boldsymbol{\tau}^p, \boldsymbol{\varpi}^p) = \overline{\mathbf{E}} \cdot \langle \boldsymbol{\varpi}^p \rangle. \tag{17}$$

which differs from problem (15) only by the space to which the trial and test functions belong. Since the dimension of $\mathbb{V}^p$ is finite, solving problem (17) amounts to solving a linear system. The resulting solution $\boldsymbol{\tau}^p$ approximates the solution to the initial problem (15).

The variational form of the EIM results from the specialization of the above procedure to matrix-inhomogeneity media, and a specific class of discretization spaces $\mathbb{V}^p$. We therefore consider a spherical RVE $\Omega \subset \mathbb{R}^3$ that hosts N inhomogeneities $\Omega_1, \ldots, \Omega_N$ embedded in a homogeneous matrix Ω_0. The inhomogeneities do not overlap. Therefore, $\Omega_0, \Omega_1, \ldots, \Omega_N$ realize a partition of the RVE Ω; the corresponding indicator functions χ_α ($\alpha = 0, \ldots, N$) are

$$\chi_\alpha(\mathbf{x}) = \begin{cases} 1 & \text{if } \mathbf{x} \in \Omega_\alpha, \\ 0 & \text{otherwise.} \end{cases} \tag{18}$$

It will be convenient to introduce volume averages over inhomogeneity Ω_α

$$\langle \bullet \rangle_\alpha = \frac{1}{V_\alpha} \int_{\Omega_\alpha} \bullet(\mathbf{x}) \, \mathrm{d}^3\mathbf{x}, \tag{19}$$

where V_α denotes the volume of Ω_α. Finally, $f_\alpha = V_\alpha / V$ denotes the volume fraction occupied by inhomogeneity α within the RVE. It results from these definitions that, for a quantity $\bullet$ that vanishes over the matrix Ω_0,

$$\langle \bullet \rangle = f_0 \langle \bullet \rangle_0 + \sum_{\alpha=1}^{N} f_\alpha \langle \bullet \rangle_\alpha. \tag{20}$$

Within the framework of the EIM, the reference material must coincide with the matrix. In other words, the RVE Ω is embedded in an infinite, homogeneous material with same conductivity $\boldsymbol{\sigma}_0$ as the matrix. Similarly, each inhomogeneity $\alpha = 1, \ldots, N$ has homogeneous conductivity $\boldsymbol{\sigma}_\alpha$. The local conductivity $\boldsymbol{\sigma}(\mathbf{x})$ can therefore be expressed as

$$\boldsymbol{\sigma}(\mathbf{x}) = \chi_0(\mathbf{x}) \, \boldsymbol{\sigma}_0 + \chi_1(\mathbf{x}) \, \boldsymbol{\sigma}_1 + \ldots + \chi_N(\mathbf{x}) \, \boldsymbol{\sigma}_N, \tag{21}$$

and we have in particular

$$\langle \boldsymbol{\sigma} \rangle_\alpha = \boldsymbol{\sigma}_\alpha, \quad \text{for all} \quad \alpha = 0, \ldots, N. \tag{22}$$

The discretization space $\mathbb{V}^p$ is generated by a finite number of linearly independent functions supported on the inhomogeneities. More precisely, we seek the following decomposition for the trial function $\boldsymbol{\tau}^p$

$$\boldsymbol{\tau}^p(\mathbf{x}) = \sum_{\alpha=1}^{N} \sum_{k=0}^{K_p - 1} \tau_\alpha^k \boldsymbol{\Psi}_\alpha^k(\mathbf{x}), \tag{23}$$

where $\boldsymbol{\Psi}_\alpha^k$ is a vector shape function supported in Ω_α, and τ_α^k are scalar unknowns in $\mathbb{R}$. $K_p \in \mathbb{N}$ must be specified.

Unless otherwise noted, greek indices $(\alpha, \beta, \ldots)$ span the $1, \ldots N$ range in the remainder of this paper (note that the matrix $\alpha = 0$ is *not* included in the sum), while latin indices $(k, l, \ldots)$ span the $0, \ldots K_p - 1$ range.

Typically, the $\boldsymbol{\Psi}_\alpha^k$ might be identical for $k = 0, \ldots, K_p - 1$ up to a rigid body motion (see below): $\boldsymbol{\Psi}_\alpha^k = \boldsymbol{\Psi}^k \circ \mathbf{F}_\alpha$, where $\mathbf{F}_\alpha$ is an isometry of $\mathbb{R}^3$. Since the $\boldsymbol{\Psi}_\alpha^k$ are supported in Ω_α, we have

$$\langle \boldsymbol{\Psi}_\alpha^k \rangle_\beta = 0 \quad \text{for all} \quad \beta = 0, \ldots, N \quad \text{such that} \quad \beta \neq \alpha. \tag{24}$$

Plugging this decomposition into the discrete variational problem (17), and testing with test functions $\boldsymbol{\varpi}^p \in \mathbb{V}^p$ decomposed similarly

$$\boldsymbol{\varpi}^p(\mathbf{x}) = \sum_\alpha \sum_k \varpi_\alpha^k \boldsymbol{\Psi}_\alpha^k(\mathbf{x}), \tag{25}$$

the following linear system is derived in Appendix B

$$\sum_l R_\alpha^{kl} \tau_\alpha^l + \sum_{\beta,l} (T_{\alpha\beta}^{kl} - f_\beta \mathbf{M}_\alpha^k \cdot \mathbf{P}_0 \cdot \mathbf{M}_\beta^l) \tau_\beta^l = \mathbf{M}_\alpha^k \cdot \overline{\mathbf{E}}, \tag{26}$$

where

$$R_\alpha^{kl} = \langle \boldsymbol{\Psi}_\alpha^k \cdot (\boldsymbol{\sigma}_\alpha - \boldsymbol{\sigma}_0)^{-1} \cdot \boldsymbol{\Psi}_\alpha^l \rangle_\alpha, \tag{27}$$

$$T_{\alpha\beta}^{kl} = \langle \boldsymbol{\Psi}_\alpha^k \cdot \boldsymbol{\Gamma}_0^\infty(\boldsymbol{\Psi}_\beta^l) \rangle_\alpha, \tag{28}$$

$$\mathbf{M}_\alpha^k = \langle \boldsymbol{\Psi}_\alpha^k \rangle_\alpha. \tag{29}$$

When $\alpha \neq \beta$, $T_{\alpha\beta}^{kl}$ represents the $\boldsymbol{\Psi}_\alpha^k$-weighted average of the (opposite of the) electric field induced on inclusion α by the polarization $\boldsymbol{\Psi}_\beta^l$ applied to inclusion β. Hence, $T_{\alpha\beta}^{kl}$ will be called *interaction coefficient*.

When $\alpha = \beta$, $T_{\alpha\alpha}^{kl}$ represents the $\boldsymbol{\Psi}_\alpha^k$-weighted average of the (opposite of the) electric field induced on inclusion α by the polarization $\boldsymbol{\Psi}_\alpha^l$ applied to the *same* inclusion α. Then, we note $T_{\alpha\alpha}^{kl} = S_\alpha^{kl}$ and S_α^{kl} will be called *self-influence coefficient*.

Gathering the $\alpha = \beta$ terms in Eq. (26) finally delivers the set of $N \times K_p$ linear equations

$$\sum_l [R_\alpha^{kl} + S_\alpha^{kl} - f_\alpha \mathbf{M}_\alpha^k \cdot \mathbf{P}_0 \cdot \mathbf{M}_\alpha^l] \tau_\alpha^l + \sum_{\beta \neq \alpha, l} (T_{\alpha\beta}^{kl} - f_\beta \mathbf{M}_\alpha^k \cdot \mathbf{P}_0 \cdot \mathbf{M}_\beta^l) \tau_\beta^l = \mathbf{M}_\alpha^k \cdot \overline{\mathbf{E}}, \tag{30}$$

which form the EIM. Finally, Eq. (14) is applied to the solution to the above linear system to derive the EIM estimate of the apparent conductivity, $\boldsymbol{\sigma}^{\mathrm{EIM}}$

$$\boldsymbol{\sigma}^{\mathrm{EIM}} \cdot \overline{\mathbf{E}} = \boldsymbol{\sigma}_0 \cdot \overline{\mathbf{E}} + \sum_{\alpha,k} f_\alpha \tau_\alpha^k \mathbf{M}_\alpha^k. \tag{31}$$

2.3. Integral expression of the interaction and self-influence coefficients

In the present section, we combine Eq. (28), which defines the influence coefficients, with Eq. (10), which gives an integral expression of the Green operator. We start from Eq. (28)

$$T_{\alpha\beta}^{kl} = \langle \boldsymbol{\Psi}_\alpha^k \cdot \boldsymbol{\Gamma}_0^\infty(\boldsymbol{\Psi}_\beta^l) \rangle_\alpha = \frac{1}{V_\alpha} \int_{\mathbf{y}_\alpha \in \Omega_\alpha} \boldsymbol{\Psi}_\alpha^k(\mathbf{y}_\alpha) \cdot \boldsymbol{\Gamma}_0^\infty(\boldsymbol{\Psi}_\beta^l) \, \mathrm{d}^3 \mathbf{y}_\alpha, \tag{32}$$

we then use Eq. (10) (assuming the reference material to be isotropic)

$$T_{\alpha\beta}^{kl} = \frac{1}{3\sigma_0} \langle \boldsymbol{\Psi}_\alpha^k \cdot \boldsymbol{\Psi}_\beta^l \rangle_\alpha + \frac{1}{V_\alpha} \int_{\mathbf{y}_\alpha \in \Omega_\alpha} \boldsymbol{\Psi}_\alpha^k(\mathbf{y}_\alpha) \cdot \operatorname*{PV}_{\mathbf{y}_\alpha} \int_{\mathbf{y}_\beta \in \Omega_\beta} \mathbf{G}_0(\mathbf{y}_\beta - \mathbf{y}_\alpha) \cdot \boldsymbol{\Psi}_\beta^l(\mathbf{y}_\beta) \, \mathrm{d}^3 \mathbf{y}_\beta \mathrm{d}^3 \, \mathbf{y}_\alpha, \tag{33}$$

where it is noted that the nested integral is performed over Ω_β, rather than Ω, owing to $\boldsymbol{\Psi}_\beta^l$ being supported in these domains. At this point, two cases must be discussed.

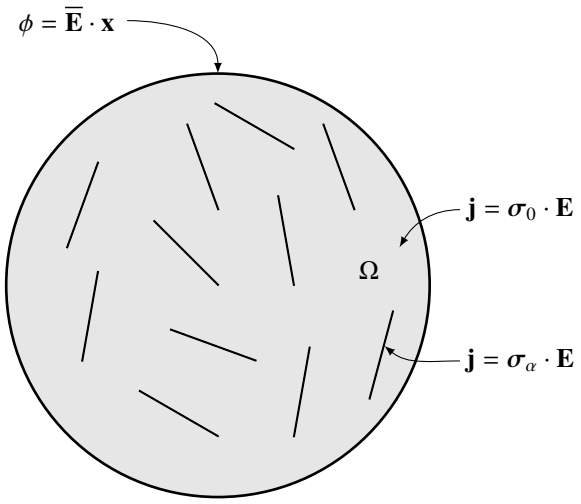

Figure 1: Determination of the apparent conductivity of the RVE Ω requires the solution to the boundary value problem (1), (2) and (3), as depicted in the above sketch.

Interaction coefficients. When $\alpha \neq \beta$, the inhomogenities Ω_α and Ω_β do not overlap. Since $\boldsymbol{\Psi}^k_\alpha \cdot \boldsymbol{\Psi}^l_\beta$ is supported in $\Omega_\alpha \cap \Omega_\beta = \emptyset$, its volume average vanishes. Furthermore, the nested integral in Eq. (33) is regular. We therefore have the following expression of the interaction coefficient

$$T^{kl}_{\alpha\beta} = \frac{1}{V_\alpha} \int_{\mathbf{y}_\alpha \in \Omega_\alpha} \int_{\mathbf{y}_\beta \in \Omega_\beta} \boldsymbol{\Psi}^k_\alpha(\mathbf{y}_\alpha) \cdot \mathbf{G}_0(\mathbf{y}_\beta - \mathbf{y}_\alpha) \cdot \boldsymbol{\Psi}^l_\beta(\mathbf{y}_\beta) \, \mathrm{d}^3\mathbf{y}_\beta \, \mathrm{d}^3\mathbf{y}_\alpha. \tag{34}$$

Furthermore, for isotropic reference materials, Eq. (10) applies, and

$$T^{kl}_{\alpha\beta} = \sigma_0^{-1}(U^{kl}_{\alpha\beta} - V^{kl}_{\alpha\beta}), \tag{35}$$

with

$$U^{kl}_{\alpha\beta} = \frac{1}{4\pi \, V_\alpha} \int_{\mathbf{y}_\alpha \in \Omega_\alpha} \int_{\mathbf{y}_\beta \in \Omega_\beta} \frac{\boldsymbol{\Psi}^k_\alpha(\mathbf{y}_\alpha) \cdot \boldsymbol{\Psi}^l_\beta(\mathbf{y}_\beta)}{\|\mathbf{y}_\beta - \mathbf{y}_\alpha\|^3} \, \mathrm{d}^3\mathbf{y}_\beta \, \mathrm{d}^3\mathbf{y}_\alpha, \tag{36}$$

and

$$V^{kl}_{\alpha\beta} = \frac{3}{4\pi \, V_\alpha} \int_{\mathbf{y}_\alpha \in \Omega_\alpha} \int_{\mathbf{y}_\beta \in \Omega_\beta} \frac{[\boldsymbol{\Psi}^k_\alpha(\mathbf{y}_\alpha) \cdot (\mathbf{y}_\beta - \mathbf{y}_\alpha)][(\mathbf{y}_\beta - \mathbf{y}_\alpha) \cdot \boldsymbol{\Psi}^l_\beta(\mathbf{y}_\beta)]}{\|\mathbf{y}_\beta - \mathbf{y}_\alpha\|^5} \, \mathrm{d}^3\mathbf{y}_\alpha \, \mathrm{d}^3\mathbf{y}_\beta. \tag{37}$$

Self-influence coefficient. When $\alpha = \beta$, the principal value cannot be removed

$$S^{kl}_\alpha = \frac{Q^{kl}_\alpha}{3\sigma_0} + \frac{1}{V_\alpha} \int_{\mathbf{x} \in \Omega_\alpha} \boldsymbol{\Psi}^k_\alpha(\mathbf{x}) \cdot \operatorname*{PV}_{\mathbf{x}} \int_{\mathbf{y} \in \Omega_\alpha} \mathbf{G}_0(\mathbf{y} - \mathbf{x}) \cdot \boldsymbol{\Psi}^l_\alpha(\mathbf{y}) \, \mathrm{d}^3\mathbf{y} \, \mathrm{d}^3\mathbf{x}, \quad \text{where} \quad Q^{kl}_\alpha = \langle \boldsymbol{\Psi}^k_\alpha \cdot \boldsymbol{\Psi}^l_\alpha \rangle_\alpha. \tag{38}$$

The EIM introduced in the previous section applies to inhomogeneities of arbitrary shape. For spherical inhomogeneities, all spatial coordinates are equivalent. Therefore Brisard et al. [7] considered polarizations that were, over each inhomogeneity, polynomial of *all* spatial coordinates. In two dimensions, such choice delivered accurate estimates of the effective properties for a relatively low number of unknowns. However, this approach was found to be inefficient in three dimensions, where polynomials of higher order were required, which led to an unacceptable growth of the number of unknowns (curse of dimensionality). For slender, cylindrical heterogeneities, the polynomial expansions are not required to be of the same order in the longitudinal and transverse directions, which alleviates this limitation. This is discussed in the next section.

3. The EIM for slender, cylindrical inhomogeneities

In the present section, the EIM described previously is specialized to slender, cylindrical inhomogeneities. In Sec. 3.1, the discretization space is defined. It is emphasized that the longitudinal coordinate (along the axis of the cylinder) plays a specific role. Then, an asymptotic expansion of the interaction coefficients is derived and evaluated numerically in Sec. 3.2. The finite element method is finally used to precompute the self-influence coefficients in Sec. 3.3.

3.1. The discretization space

For the sake of simplicity, *monodisperse* assemblies only will be considered in the derivations presented below, and we introduce the common radius R and common total length $2L$ of the cylindrical inhomogeneities. Then, Ω_α is a circular cylinder centered at $\mathbf{x}_\alpha \in \Omega$, oriented by the unit-vector $\mathbf{n}_\alpha$ (see Fig. 2). The aspect ratio e of the cylinders is defined as: $e = L/R$. For such inhomogeneities, the longitudinal coordinate z_α defined as follows

$$z_\alpha = (\mathbf{x} - \mathbf{x}_\alpha) \cdot \mathbf{n}_\alpha \tag{39}$$

clearly plays a specific role. This suggests to consider polarizations that are polynomials of high-order p of the longitudinal coordinate, and polynomials of low-order q of the two other, transverse, coordinates. Typically, $q = 0, 1, 2$; owing to the large slenderness of the cylinders that will be considered in the applications, the simplest case $q = 0$ is investigated first. In other words, the discretization space $\mathbb{V}^p$ is now the space of tensor fields that are, over each inhomogeneity Ω_α, polynomial of the local longitudinal coordinate z_α. The general decomposition (23) of the trial function $\boldsymbol{\tau}^p$ therefore applies, p is the degree of polynoms and the total number of scalar unknowns is $K_p = 3(p + 1)$.

Introducing the following scalar shape functions of order $m \leq p$

$$\psi_\alpha^m(\mathbf{x}) = \chi_\alpha(\mathbf{x}) z_\alpha^m, \tag{40}$$

the vector shape functions are indexed as follows

$$\boldsymbol{\Psi}_\alpha^{(p+1)(i-1)+m}(\mathbf{x}) = \psi_\alpha^m(\mathbf{x})\, \mathbf{e}_i \quad (i = 1, 2, 3). \tag{41}$$

where $(\mathbf{e}_1, \mathbf{e}_2, \mathbf{e}_3)$ is the global cartesian frame. Note that in the above indexing scheme, the polynomial order is the "fast" index, while the spatial direction of the polarization ($i = 1, 2, 3$) is the "slow" index.

For $0 \leq k < K_p$, it will be convenient to introduce the functions $0 \leq \mathcal{O}(k) \leq p$ and $1 \leq \mathcal{D}(k) \leq 3$ defined as follows: $\mathcal{D}(k) - 1$ (resp. $\mathcal{O}(k)$) is the quotient (resp. remainder) of the Euclidean division of k by $(p + 1)$

$$k = (p + 1)[\mathcal{D}(k) - 1] + \mathcal{O}(k). \tag{42}$$

The geometric moment $\mathbf{M}_\alpha^k$ introduced in Eq. (29) reduces to

$$\mathbf{M}_\alpha^k = M_\alpha^{\mathcal{O}(k)} \mathbf{e}_{\mathcal{D}(k)}, \quad \text{with} \quad M_\alpha^m = \frac{1}{V_\alpha} \int_{\mathbf{x} \in \Omega_\alpha} z_\alpha^m \, \mathrm{d}^3\mathbf{x} \quad (0 \leq m \leq p) \tag{43}$$

and, if $\boldsymbol{\sigma}_\alpha$ is isotropic ($\boldsymbol{\sigma}_\alpha = \sigma_\alpha \, \mathbf{1}$), we have

$$R_\alpha^{kl} = (\sigma_\alpha - \sigma_0)^{-1} Q_\alpha^{kl}, \quad \text{with} \quad Q_\alpha^{kl} = \delta_{\mathcal{D}(k)\,\mathcal{D}(l)} M_\alpha^{\mathcal{O}(k)+\mathcal{O}(l)} \tag{44}$$

where δ_{ij} is the Kronecker symbol. Note that, for circular cylinders

$$M_\alpha^m = \frac{1 + (-1)^m}{2(m + 1)} L^m. \tag{45}$$

For the practical implementation of the method, it will prove convenient to write the interaction and self-influence coefficents in a matrix form

$$\mathsf{T}_{\alpha\beta}^{mn} = \begin{pmatrix} T_{\alpha\beta}^{m,n} & T_{\alpha\beta}^{m,n+p+1} & T_{\alpha\beta}^{m,n+2(p+1)} \\ T_{\alpha\beta}^{m+p+1,n} & T_{\alpha\beta}^{m+p+1,n+p+1} & T_{\alpha\beta}^{m+p+1,n+2(p+1)} \\ T_{\alpha\beta}^{m+2(p+1),n} & T_{\alpha\beta}^{m+2(p+1),n+p+1} & T_{\alpha\beta}^{m+2(p+1),n+2(p+1)} \end{pmatrix} \tag{46}$$

and

$$\mathsf{S}_{\alpha}^{mn} = \begin{pmatrix} S_{\alpha}^{m,n} & S_{\alpha}^{m,n+p+1} & S_{\alpha}^{m,n+2(p+1)} \\ S_{\alpha}^{m+p+1,n} & S_{\alpha}^{m+p+1,n+p+1} & S_{\alpha}^{m+p+1,n+2(p+1)} \\ S_{\alpha}^{m+2(p+1),n} & S_{\alpha}^{m+2(p+1),n+p+1} & S_{\alpha}^{m+2(p+1),n+2(p+1)} \end{pmatrix} \tag{47}$$

with $0 \leq m, n \leq p$. In the remainder of this paper, latin, superior indices to the matrices T and S will always be assumed to span $0, ..., p$.

3.2. Computation of the interaction coefficients

For two distinct inhomogeneities $\alpha \neq \beta$, Eq. (35) can be replaced with

$$\mathsf{T}_{\alpha\beta}^{mn} = \sigma_0^{-1}(U_{\alpha\beta}^{mn}\mathsf{I}_3 - \mathsf{V}_{\alpha\beta}^{mn}), \tag{48}$$

where I_3 is the 3×3 identity matrix, and

$$U_{\alpha\beta}^{mn} = \frac{1}{4\pi\, V_\alpha} \int_{\mathbf{y}_\alpha \in \Omega_\alpha} \int_{\mathbf{y}_\beta \in \Omega_\beta} \frac{z_\alpha^m\, z_\beta^n}{\|\mathbf{y}_\beta - \mathbf{y}_\alpha\|^3}\, \mathrm{d}^3\mathbf{y}_\beta\, \mathrm{d}^3\mathbf{y}_\alpha, \tag{49}$$

and the coefficients of $\mathsf{V}_{\alpha\beta}^{mn}$ are

$$\left(\mathsf{V}_{\alpha\beta}^{mn}\right)_{ij} = \frac{3}{4\pi\, V_\alpha} \int_{\mathbf{y}_\alpha \in \Omega_\alpha} \int_{\mathbf{y}_\beta \in \Omega_\beta} z_\alpha^m\, z_\beta^n \frac{[(\mathbf{y}_\beta - \mathbf{y}_\alpha)\cdot\mathbf{e}_i][(\mathbf{y}_\beta - \mathbf{y}_\alpha)\cdot\mathbf{e}_j]}{\|\mathbf{y}_\beta - \mathbf{y}_\alpha\|^5}\, \mathrm{d}^3\mathbf{y}_\beta\, \mathrm{d}^3\mathbf{y}_\alpha, \tag{50}$$

for $i, j = 1, 2, 3$.

We were not able to derive a closed-form expression of these integrals for two cylinders. However, assuming that the radius R is small compared to the smallest distance between the two cylinders, a multipole expansion can be produced. For low volume fractions, this assumption is certainly verified for most pairs of cylinders. We introduce the local cylindrical coordinates $(r_\alpha, \theta_\alpha, z_\alpha)$ and $(r_\beta, \theta_\beta, z_\beta)$ (see Fig. 2)

$$\mathbf{y}_\alpha = \mathbf{x}_\alpha + z_\alpha \mathbf{n}_\alpha + r_\alpha \mathbf{e}_{r,\alpha}, \tag{51}$$

where $\mathbf{e}_{r,\alpha}$ is the unit radial vector, while θ_α is the polar angle with respect to a fixed (unspecified) direction. The integral for $\mathsf{U}_{\alpha\beta}^{KM}$ then reads

$$U_{\alpha\beta}^{mn} = \frac{1}{4\pi\, V_\alpha} \int_{\substack{0\leq r_\alpha, r_\beta \leq R \\ 0\leq\theta_\alpha,\theta_\beta\leq 2\pi \\ -L\leq z_\alpha, z_\beta \leq L}} \frac{r_\alpha\, r_\beta\, z_\alpha^m\, z_\beta^n}{\|\mathbf{w}\|^3}\, \mathrm{d}z_\alpha\, \mathrm{d}z_\beta\, \mathrm{d}\theta_\alpha\, \mathrm{d}\theta_\beta\, \mathrm{d}r_\alpha\, \mathrm{d}r_\beta, \tag{52}$$

and

$$\left(\mathsf{V}_{\alpha\beta}^{mn}\right)_{ij} = \frac{3}{4\pi\, V_\alpha} \int_{\substack{0\leq r_\alpha, r_\beta \leq R \\ 0\leq\theta_\alpha,\theta_\beta\leq 2\pi \\ -L\leq z_\alpha, z_\beta \leq L}} \frac{r_\alpha\, r_\beta\, z_\alpha^m\, z_\beta^n\, w_i\, w_j}{\|\mathbf{w}\|^5}\, \mathrm{d}z_\alpha\, \mathrm{d}z_\beta\, \mathrm{d}\theta_\alpha\, \mathrm{d}\theta_\beta\, \mathrm{d}r_\alpha\, \mathrm{d}r_\beta, \tag{53}$$

where $\mathbf{w}$ stands for the following vector

$$\mathbf{w} = \mathbf{r}_{\alpha\beta} + z_\beta \mathbf{n}_\beta - z_\alpha \mathbf{n}_\alpha + r_\beta \mathbf{e}_{r,\beta} - r_\alpha \mathbf{e}_{r,\alpha}, \tag{54}$$

with $\mathbf{r}_{\alpha\beta} = \mathbf{x}_\beta - \mathbf{x}_\alpha$. In view of performing an asymptotic expansion of the above integrals, we introduce the following dimensionless variables

$$\zeta_\alpha = \frac{z_\alpha}{L}, \quad \zeta_\beta = \frac{z_\beta}{L}, \quad \rho_\alpha = \frac{r_\alpha}{R}, \quad \text{and} \quad \rho_\beta = \frac{r_\beta}{R}. \tag{55}$$

Observing that the volume of inhomogeneity α is $V_\alpha = 2\pi R^2 L$, we get

$$U_{\alpha\beta}^{mn} = \frac{L^{m+n+3}}{8\pi^2}\frac{R^2}{L^2}\int_{\substack{0\le\rho_\alpha,\rho_\beta\le 1\\ 0\le\theta_\alpha,\theta_\beta\le 2\pi\\ -1\le\zeta_\alpha,\zeta_\beta\le 1}} \frac{\rho_\alpha\,\rho_\beta\,\zeta_\alpha^m\,\zeta_\beta^n}{\|\mathbf{w}\|^3}\,\mathrm{d}\zeta_\alpha\,\mathrm{d}\zeta_\beta\,\mathrm{d}\theta_\alpha\,\mathrm{d}\theta_\beta\,\mathrm{d}\rho_\alpha\,\mathrm{d}\rho_\beta, \tag{56}$$

$$\left(\mathsf{V}_{\alpha\beta}^{mn}\right)_{ij} = \frac{3L^{m+n+3}}{8\pi^2}\frac{R^2}{L^2}\int_{\substack{0\le\rho_\alpha,\rho_\beta\le 1\\ 0\le\theta_\alpha,\theta_\beta\le 2\pi\\ -1\le\zeta_\alpha,\zeta_\beta\le 1}} \frac{\rho_\alpha\,\rho_\beta\,\zeta_\alpha^m\,\zeta_\beta^n\,w_i\,w_j}{\|\mathbf{w}\|^5}\,\mathrm{d}\zeta_\alpha\,\mathrm{d}\zeta_\beta\,\mathrm{d}\theta_\alpha\,\mathrm{d}\theta_\beta\,\mathrm{d}\rho_\alpha\,\mathrm{d}\rho_\beta, \tag{57}$$

where

$$\mathbf{w} = L\zeta_\beta\mathbf{n}_\beta - L\zeta_\alpha\mathbf{n}_\alpha + \mathbf{r}_{\alpha\beta} + R(\rho_\beta\mathbf{e}_{r,\beta} - \rho_\alpha\mathbf{e}_{r,\alpha}). \tag{58}$$

Owing to our assumption that the radius of the cylinders is small compared to the smallest cylinder-to-cylinder distance, it is observed that $R\|\rho_\beta\mathbf{e}_{r,\beta} - \rho_\alpha\mathbf{e}_{r,\alpha}\| \ll \|L\zeta_\beta\mathbf{n}_\beta - L\zeta_\alpha\mathbf{n}_\alpha + \mathbf{r}_{\alpha\beta}\|$ in the above expression. Then

$$U_{\alpha\beta}^{mn} = \frac{L^{m+n+3}}{8\pi^2}\frac{R^2}{L^2}\int \frac{\rho_\alpha\,\rho_\beta\,\zeta_\alpha^m\,\zeta_\beta^n}{\|\mathbf{w}^0\|^3}\,\mathrm{d}\zeta_\alpha\,\mathrm{d}\zeta_\beta\,\mathrm{d}\theta_\alpha\,\mathrm{d}\theta_\beta\,\mathrm{d}\rho_\alpha\,\mathrm{d}\rho_\beta, \tag{59}$$

$$\left(\mathsf{V}_{\alpha\beta}^{mn}\right)_{ij} = \frac{3L^{m+n+3}}{8\pi^2}\frac{R^2}{L^2}\int \frac{\rho_\alpha\,\rho_\beta\,\zeta_\alpha^m\,\zeta_\beta^n w_i^0 w_j^0}{\|\mathbf{w}^0\|^5}\,\mathrm{d}\zeta_\alpha\,\mathrm{d}\zeta_\beta\,\mathrm{d}\theta_\alpha\,\mathrm{d}\theta_\beta\,\mathrm{d}\rho_\alpha\,\mathrm{d}\rho_\beta, \tag{60}$$

where the integration bounds have been omitted and

$$\mathbf{w}^0 = \mathbf{r}_{\alpha\beta} + L\zeta_\beta\mathbf{n}_\beta - L\zeta_\alpha\mathbf{n}_\alpha. \tag{61}$$

Upon integration with respect to $0 \le \rho_\alpha, \rho_\beta \le 1$ and $0 \le \theta_\alpha, \theta_\beta \le 2\pi$

$$U_{\alpha\beta}^{mn} = \frac{L^{m+n+3}}{8}\frac{R^2}{L^2}\int_{-1}^{1}\int_{-1}^{1} \frac{\zeta_\alpha^m\,\zeta_\beta^n}{\|\mathbf{w}^0\|^3}\,\mathrm{d}\zeta_\alpha\,\mathrm{d}\zeta_\beta, \tag{62}$$

$$\left(\mathsf{V}_{\alpha\beta}^{mn}\right)_{ij} = \frac{3L^{m+n+3}}{8}\frac{R^2}{L^2}\int_{-1}^{1}\int_{-1}^{1} \frac{\zeta_\alpha^m\,\zeta_\beta^n w_i^0 w_j^0}{\|\mathbf{w}^0\|^5}\mathrm{d}\zeta_\alpha\,\mathrm{d}\zeta_\beta. \tag{63}$$

In the above expressions, both nested integrals can be evaluated numerically. However, this method becomes inefficient for a large number of inclusions, in which case it is more advantageous to evaluate the first integral (with respect to ζ_α) analytically. More details are provided in a report by Martin [21], available at https://hal.archives-ouvertes.fr/hal-03736626 (last retrieved 2023-01-11).

3.3. Computation of the self-influence coefficients

Eq. (38) shows that the singularity cannot be removed in the integral expression of the self-influence coefficients, which makes their analytical evaluation difficult. Rather than attempting a regularized quadrature, and observing that this coefficient can be precomputed off-line prior to the full EIM calculation, we used a numerical approach based on a finite element analysis.

It is recalled (see Sec. 2.2) that $(\mathsf{S}_\alpha^{mn})_{ij} = -\langle\psi_\alpha^m\mathbf{e}_i\cdot\mathbf{grad}\,\phi\rangle_\alpha$, where ϕ is the electric potential induced by the polarization $\psi_\alpha^n\mathbf{e}_j$ in Ω_α. In other words, we consider the solution to the following variational problem over $\mathbb{R}^3$: find ϕ such that, for all $\hat{\phi}$

$$\int_{\mathbb{R}^3}\sigma_0\,\mathbf{grad}\,\phi\cdot\mathbf{grad}\,\hat{\phi} + \int_{\Omega_\alpha}\psi_\alpha^n\mathbf{e}_j\cdot\mathbf{grad}\,\hat{\phi} = 0, \tag{64}$$

where ϕ and $\hat{\phi}$ are square integrable over $\mathbb{R}^3$, with square integrable gradients. In the above variational problem, it is assumed that the reference material is isotropic ($\boldsymbol{\sigma}_0 = \sigma_0\mathbf{1}$).

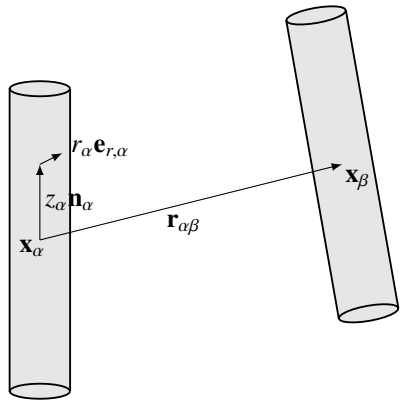

Figure 2: Computation of the interaction coefficients

The domain Ω_α is axisymmetric, but the loading (the polarization), which depends on $\mathbf{e}_j$ is not. Still, it is possible to reduce the above 3d problem to a finite set of 2d problems [35, 27]. Indeed, introducing the cylindrical coordinates (r, θ, z) within Ω_α, and a local cartesian basis $(\mathbf{g}_1, \mathbf{g}_2, \mathbf{g}_3)$ where $\mathbf{g}_3 = \mathbf{n}_\alpha$, we have

$$\mathbf{e}_j = [(\mathbf{e}_j \cdot \mathbf{g}_1)\cos\theta + (\mathbf{e}_j \cdot \mathbf{g}_2)\sin\theta]\mathbf{e}_r + [-(\mathbf{e}_j \cdot \mathbf{g}_1)\sin\theta + (\mathbf{e}_j \cdot \mathbf{g}_2)\cos\theta]\mathbf{e}_\theta + (\mathbf{e}_j \cdot \mathbf{g}_3)\mathbf{e}_z. \tag{65}$$

Note that ψ_α^n does not depend on θ, which suggests the following form of the solution, in cylindrical coordinates

$$\phi(r, \theta, z) = \Phi_1(r, z)[(\mathbf{e}_j \cdot \mathbf{g}_1)\cos\theta + (\mathbf{e}_j \cdot \mathbf{g}_2)\sin\theta] + (\mathbf{e}_j \cdot \mathbf{g}_3)\Phi_3(r, z), \tag{66}$$

where Φ_1 and Φ_3 are two functions of (r, z) only, to be determined.

Plugging the expansion (66) into the 3d variational problem (64) and testing with $\hat{\Phi}(r, z)\cos\theta$, $\hat{\Phi}(r, z)\sin\theta$ and $\hat{\Phi}(r, z)$, successively ($\hat{\Phi}$: arbitrary function of r and z only) delivers the following 2d variational problems upon integration with respect to $0 \le \theta \le 2\pi$: find Φ_1 and Φ_3 such that, for all $\hat{\Phi}$

$$\sigma_0 \int_{-\infty}^{+\infty}\int_0^{+\infty}\left[r\left(\frac{\partial\Phi_1}{\partial r}\frac{\partial\hat{\Phi}}{\partial r} + \frac{\partial\Phi_1}{\partial z}\frac{\partial\hat{\Phi}}{\partial z}\right) + \frac{\Phi_1\hat{\Phi}}{r}\right]\mathrm{d}r\,\mathrm{d}z + \int_{-L}^{+L}\int_0^R \psi_\alpha^n(z)\left(\hat{\Phi} + r\frac{\partial\hat{\Phi}}{\partial r}\right)\mathrm{d}r\,\mathrm{d}z = 0 \tag{67}$$

and

$$\sigma_0 \int_{-\infty}^{+\infty}\int_0^{+\infty} r\left(\frac{\partial\Phi_3}{\partial r}\frac{\partial\hat{\Phi}}{\partial r} + \frac{\partial\Phi_3}{\partial z}\frac{\partial\hat{\Phi}}{\partial z}\right)\mathrm{d}r\,\mathrm{d}z + \int_{-L}^{+L}\int_0^R r\,\psi_\alpha^n(z)\frac{\partial\hat{\Phi}}{\partial z}\,\mathrm{d}r\,\mathrm{d}z = 0. \tag{68}$$

The variational problems (67) and (68) were implemented within the FEniCS framework [20, 3]. Boundary conditions at $r \to +\infty$ were replaced with Dirichlet boundary conditions at $r = 20L$ (spherical simulation domain). Then, from Φ_1 and Φ_3, S_α^{mn} is computed as follows (see Appendix C)

$$\mathsf{S}_\alpha^{mn} = S_{\alpha,\mathrm{T}}^{mn}(\mathsf{I}_3 - \mathsf{n}_\alpha\mathsf{n}_\alpha^{\mathrm{T}}) + S_{\alpha,\mathrm{L}}^{mn}\,\mathsf{n}_\alpha\mathsf{n}_\alpha^{\mathrm{T}}, \tag{69}$$

where n_α is the 3×1 column vector of the coordinates of $\mathbf{n}_\alpha$ in the global basis $(\mathbf{e}_1, \mathbf{e}_2, \mathbf{e}_3)$ and

$$S_{\alpha,\mathrm{T}}^{mn} = -\frac{1}{2R^2L}\int_{-L}^{+L}\int_0^R r\,\psi_\alpha^m\left(\frac{\partial\Phi_1}{\partial r} + \frac{\Phi_1}{r}\right)\mathrm{d}r\,\mathrm{d}z \quad \text{and} \quad S_{\alpha,\mathrm{L}}^{mn} = -\frac{1}{R^2L}\int_{-L}^{+L}\int_0^R r\,\psi_\alpha^m\frac{\partial\Phi_3}{\partial z}\,\mathrm{d}r\,\mathrm{d}z. \tag{70}$$

Remark 3. *Note that the compact expression (66) was inferred from a first analysis where the following, slightly more general, expansion was adopted*

$$\phi(r, \theta, z) = \phi_{\mathrm{c}}(r, z)\cos\theta + \phi_{\mathrm{s}}(r, z)\sin\theta + \phi_0(r, z), \tag{71}$$

and it was observed that the variational problem that ϕ_{c} (resp. ϕ_{s}, ϕ_0) solves involves $(\mathbf{e}_j \cdot \mathbf{g}_1)$ (resp. $(\mathbf{e}_j \cdot \mathbf{g}_2)$, $(\mathbf{e}_j \cdot \mathbf{g}_3)$) only and ϕ_{c} and ϕ_{s} solve the same variational problem.

Remark 4. *Adessina et al. [2, 1] recently introduced a correction to the Dirichlet boundary conditions we adopted in order to minimize finite-size effects. However, it is observed that these corrections involve the ratio of the volume of the cylindrical inhomogeneity ($V_\alpha = 2\pi R^2 L$) to the volume of the simulation domain ($\frac{4}{3}\pi(20L)^3$). Therefore these corrections are of order $1/(8000e^2)$, which is negligible. We did not apply these corrections in the present case.*

The EIM was specialized to slender, cylindrical inhomogeneities in the previous section. Performance of the resulting numerical method is assessed in the remainder of this paper. We first consider the inhomogeneity problem of Eshelby [11]. This seemingly simple problem reveals that the above defined discretization space is too small for the EIM to deliver a good estimate of the local fiels. This leads us to consider *enriched* trial polarizations.

4. Application to one-inhomogeneity system

4.1. The discretization space is too small

We consider a single inhomogeneity Ω_1 centered at the origin and embedded in a homogeneous, infinite matrix. The system is subjected to a uniform electric field $\overline{\mathbf{E}} = \overline{E}\mathbf{e}_z$ at infinity, where $\overline{E}$ is a scalar constant and $\mathbf{e}_z$ denotes the axis of revolution of the inhomogeneity. Both matrix and inhomogeneity have isotropic conductivities σ_0 and σ_1, respectively. The contrast of conductivities is $\sigma_1/\sigma_0 = 10^6$, while the aspect ratio is $L/R = 50$.

Note that in the present application, the boundary conditions apply *at infinity* and there is no need for the finite-size corrections introduced by Brisard et al. [8]. In other words, the Lippmann–Schwinger equation to be solved is [compare with Eq. (8)]

$$(\sigma_1 - \sigma_0)^{-1}\boldsymbol{\tau} + \boldsymbol{\Gamma}_0^\infty(\boldsymbol{\tau}) = \overline{\mathbf{E}}. \tag{72}$$

After EIM discretization, the above equation reduces to the following system, which involves only self-influence coefficients [compare with Eq. (30)]

$$\sum_l [(\sigma_1 - \sigma_0)^{-1} Q_\alpha^{kl} + S_\alpha^{kl}]\tau_\alpha^l = \mathbf{M}_\alpha^k \cdot \overline{\mathbf{E}}. \tag{73}$$

We compared the results of EIM with finite element calculation. This calculation was done with COMSOL Multiphysics® 5.6[2]. Here again, boundary conditions were replaced with conditions at the boundary of a large sphere (radius: $20L$). The size of the smallest element is $R/5$.

The EIM electric field is uniform within the section of the cylindrical inhomogeneity. For the sake of comparison, the FEM electric field is therefore averaged over the cross section, for various values of longitudinal coordinate z along the inhomogeneity.

The results of this comparison are shown on Fig. 3, where only the longitudinal component of the electric field is represented. EIM simulations were carried out for two values of the polynomial order: $p = 2$ and $p = 16$.

Even for a rather low polynomial order, $p = 2$, the EIM can capture the magnitude and overall variations of the electric field along the cylinder. However, its maximum value is slightly under-estimated. Furthermore, it is observed that increasing the polynomial order p does not improve the accuracy significantly. This suggests that the discretization (41) is not rich enough to ensure a good approximation of the true fields. The estimated polarization should therefore be allowed to vary within the cross-section.

It would be natural to increase the polynomial order q in the transverse direction, from $q = 0$ (the polarization is constant within the cross-section) to $q = 1$ (the polarization is affine within the cross-section), which would lead to an increase of the total number of unknowns, from $3N(p+1)$ to $9N(p+1)$. This enrichment (which, in a linear elasticity setting, is consistent with the classical beam theory) will be investigated in future work.

[2]COMSOL Multiphysics® v. 5.6. www.comsol.com. COMSOL AB, Stockholm, Sweden, last retrieved 2023-01-11.

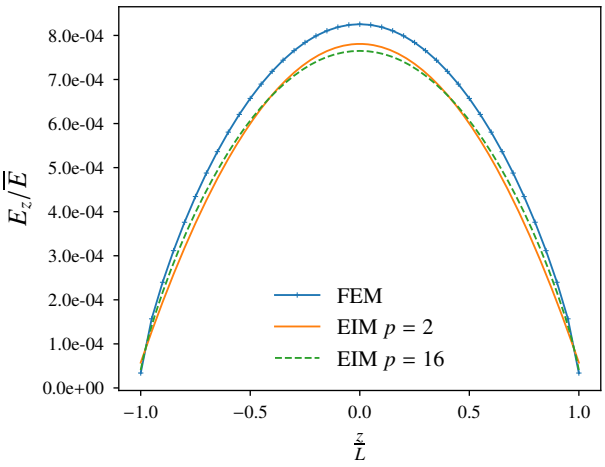

Figure 3: Eshelby's problem with contrast $\sigma_1/\sigma_0 = 10^6$ for aspect ratio $L/R = 50$. The sectional average of the longitudinal component of the electric field E_z is plotted against the longitudinal coordinate z. $\overline{E}$ is the amplitude of the longitudinal electric field, prescribed at infinity. "FEM": finite element reference simulation; "EIM $p = 2$" (resp. $p = 16$): equivalent inclusion method with polynomials of the second (resp 16th) order.

For the time being, we consider a subset of this general class of trial polarizations. To the constant polarization already considered before, we add a radial component that varies linearly with the radial distance; the total number of unknowns is therefore $4N(p+1)$ only. Figs. 4 and 5 indeed show the variations of the longitudinal (E_z) and radial (E_r) components of the FEM electric field as a function of the radial distance r, for two cross-sections: $z = 0$ (mid-height of the cylinder) and $z = L/2$ (quarter-height of the cylinder). The macroscopic (prescribed) electric field $\overline{\mathbf{E}}$ is again aligned with the cylinder axis $\mathbf{e}_z$. Note that in both figures, the values are normalized by the amplitude of the electric field at infinity. Observation of Fig. 4 (resp. 5) suggests that the longitudinal (resp. transverse) trial polarization should be allowed to vary quadratically (resp. linearly) with r. However, on closer inspection, it appears that the relative variations of E_z are significantly smaller than the relative variations of E_r, which suggests that there is no need to enrich the longitudinal component of the trial polarization, while the radial component is enriched as in the next section.

4.2. Enrichment of the trial polarization field

As discussed previously, we add to the constant trial polarization in inclusion α, a radial component, linear in r_α. Now, $K_p = 4(p+1)$ and Eq. (41) is complemented with

$$\mathbf{\Psi}_\alpha^{3(p+1)+m}(\mathbf{x}) = \psi_\alpha^m(\mathbf{x}) r_\alpha \mathbf{e}_{r,\alpha}, \tag{74}$$

where $\mathbf{e}_{r,\alpha}$ is the radial vector of cylinder α. The development of the method with this new discretization is the same as previously. The definition of $\mathcal{D}(k)$ and $O(k)$ are unchanged but for the fact that now, $\mathcal{D}(k)$ can take the value 4. In the remainder of this section, we document how the final linear system is affected by the proposed enrichment. We have

$$\mathbf{M}_\alpha^k = \mathbf{0} \quad \text{if } \mathcal{D}(k) = 4, \tag{75}$$

and

$$Q_\alpha^{kl} = \begin{cases} 0 & \text{if } [\mathcal{D}(k) = 4 \text{ or } \mathcal{D}(l) = 4] \text{ and } \mathcal{D}(k) \neq \mathcal{D}(l), \\ \dfrac{1 + (-1)^{O(k)+O(l)}}{2(O(k)+O(l)+1)} L^{O(k)+O(l)} \dfrac{R^2}{2} & \text{if } \mathcal{D}(k) = \mathcal{D}(l) = 4, \end{cases} \tag{76}$$

the other values of $\mathbf{M}_\alpha^k$ and Q_α^k being unchanged [see Eqs. (44) and (45)].

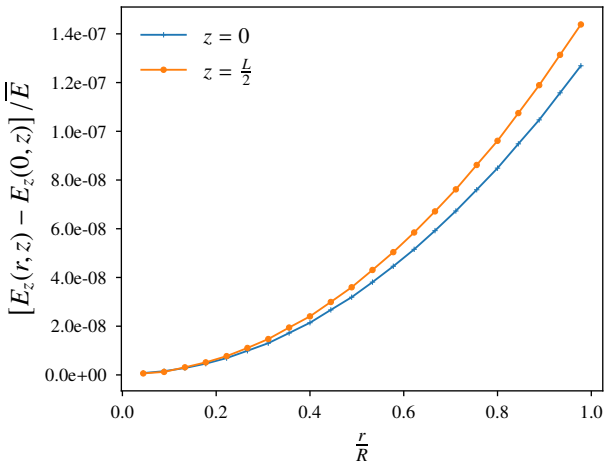

Figure 4: Variations of the longitudinal component of the electric field E_z within the cross-section of the cylinder for the problem considered in Fig. 3. Owing to rotational symmetry, E_z depends on r (distance to the cylinder's axis) and z (longitudinal coordinate) only. The curves $r \mapsto E_z$ are plotted for two values of z: $z = 0$ (mid-height) and $z = L/2$ (quarter height). $\overline{E}$ is the amplitude of the longitudinal electric field, prescribed at infinity.

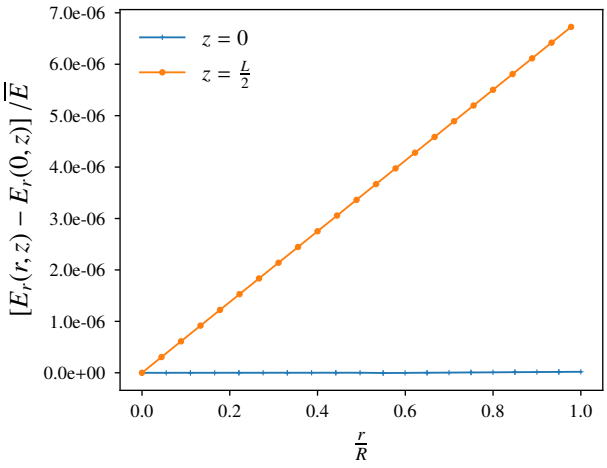

Figure 5: Variations of the radial component of the electric field E_r within the cross-section of the cylinder for the problem considered in Fig. 3. Owing to rotational symmetry, E_r depends on r (distance to the cylinder's axis) and z (longitudinal coordinate) only. The curves $r \mapsto E_z$ are plotted for two values of z: $z = 0$ (mid-height) and $z = L/2$ (quarter height). $\overline{E}$ is the amplitude of the longitudinal electric field, prescribed at infinity.

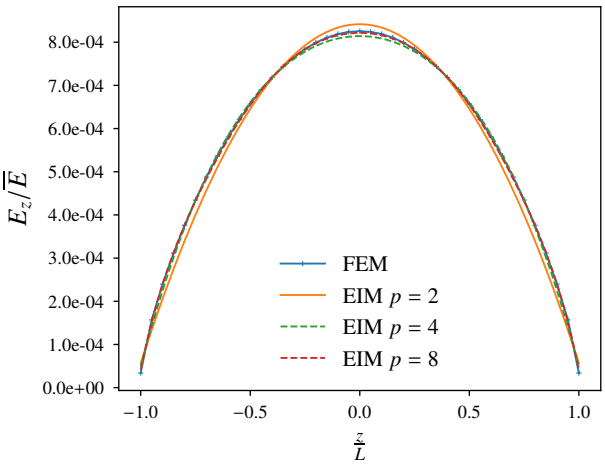

Figure 6: Eshelby's problem with contrast $\sigma_1/\sigma_0 = 10^6$ for aspect ratio $L/R = 50$. The sectional average of the longitudinal component of the electric field E_z is plotted against the longitudinal coordinate z. $\overline{E}$ is the amplitude of the longitudinal electric field, prescribed at infinity. "FEM": finite element reference simulation; "EIM $p = 2$" (resp. $p = 4$, $p = 8$): equivalent inclusion method with polynomials of order 2 (resp. 4, 8) and the enrichment (74). Comparison with Fig. 3 shows significant improvement of the solution.

It is again convenient to write the interaction and self-influence coefficents in a 4×4 matrix form, where the upper-left, 3×3 block is unchanged. We derive the expressions of the additional coefficients of S_α^{mn} and $\mathsf{T}_{\alpha\beta}^{mn}$ in Appendix D.

Fig. 6 shows the resulting approximations of the electric field for the same problem as in Sec. 4.1. The solution is significantly improved, and nearly undistinguishable from the FEM reference solution for $p \geq 8$. This is discussed in depth in the next section.

4.3. Analysis of the discretization error

In the present section, we quantify the error on the electric field resulting from the discretization of the polarization field. We define the following quantity

$$\epsilon = \left[\frac{\int_{\Omega_1} \|\mathbf{E}^{\mathrm{EIM}}(\mathbf{x}) - \mathbf{E}^{\mathrm{FEM}}(\mathbf{x})\|^2 \, \mathrm{d}^3\mathbf{x}}{\int_{\Omega_1} \|\mathbf{E}^{\mathrm{FEM}}(\mathbf{x})\|^2 \, \mathrm{d}^3\mathbf{x}} \right]^{1/2}, \tag{77}$$

which measures the relative error in L^2 norm. Here, the FEM fields were not computed with COMSOL Multiphysics® 5.6. Indeed, for high aspect ratios, the number of unknown becomes too large. Using the same technique as in Sec. 3.3, the 3d problem can however again be reduced to the following 2d variational problem (again solved with the FEniCS library): find Φ such that, for all $\hat{\Phi}$

$$\int_{-\infty}^{+\infty} \int_0^{+\infty} r\sigma \left(\frac{\partial \Phi}{\partial r} \frac{\partial \hat{\Phi}}{\partial r} + \frac{\partial \Phi}{\partial z} \frac{\partial \hat{\Phi}}{\partial z} \right) \mathrm{d}r \, \mathrm{d}z + \int_{-\infty}^{+\infty} \int_0^{+\infty} r\sigma \frac{\partial \hat{\Phi}}{\partial z} \mathrm{d}r \, \mathrm{d}z = 0. \tag{78}$$

The relative error ϵ is plotted versus the polynomial order p in Fig. 7 for a fixed aspect ratio $L/R = 50$. As expected, ϵ decreases when p increases. However, it is not guaranteed that $\epsilon \to 0$, owing to the fact that we do not increase the polynomial order q within the cross-section. Nevertheless, acceptable relative errors can be reached for relatively low polynomial orders ($p = 8$ leads to $\epsilon = 0.51\%$). This is essential for application of the proposed method to large assemblies of inclusions.

The relative error ϵ is also plotted versus the aspect ratio L/R in Fig. 8, for a fixed polynomial order $p = 8$. It is observed that the error decreases when the aspect ratio increases. This was expected, as our assumption of constant trial polarization within the cross-section targets slender cylinders.

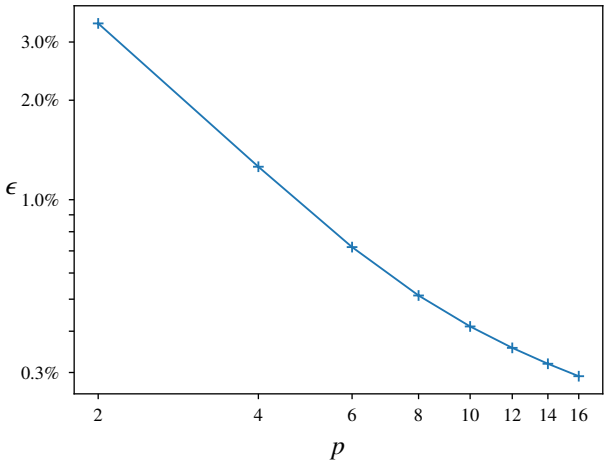

Figure 7: Eshelby's problem with contrast $\sigma_1/\sigma_0 = 10^6$ for fixed aspect ratio $L/R = 50$. The figure shows the relative error ϵ defined by Eq. (77) as a function of the polynomial order p.

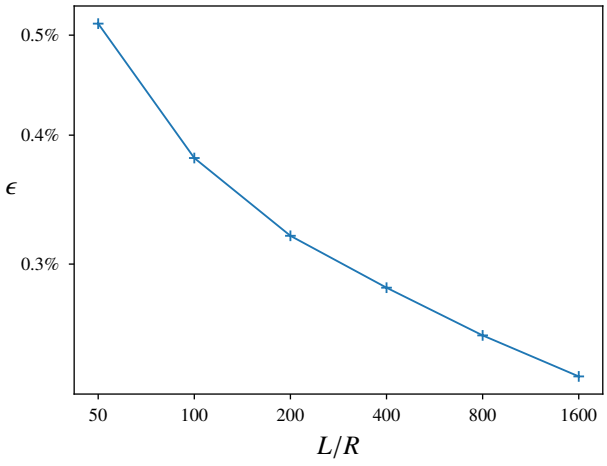

Figure 8: Eshelby's problem with contrast $\sigma_1/\sigma_0 = 10^6$ for various aspect ratios L/R. The figure shows the relative error ϵ defined by Eq. (77) for polynomials of order $p = 8$.

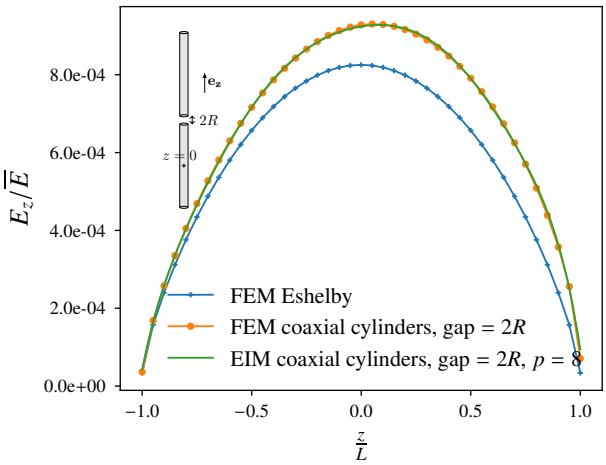

Figure 9: Two coaxial cylinders with aspect ratio $L/R = 50$ and contrast $\sigma_1/\sigma_0 = 10^6$, subjected to an external electric field $\overline{\mathbf{E}} = \overline{E}\,\mathbf{e}_z$. The gap between the cylinders is $2R$ (center-to-center distance: $2L + 2R$). The sectional average of the longitudinal component of the electric field E_z is plotted against the longitudinal coordinate z. "FEM Eshelby": finite element simulation for an isolated cylinder; "FEM coaxial cylinders": finite element reference solution; "EIM coaxial cylinders $p = 8$": equivalent inclusion method with polynomials of order 8.

It has been shown in the previous section that the EIM can deliver excellent estimates of the electric field for an isolated cylindrical inhomogeneity, provided that the trial polarization is enriched with a radial component, linear in the radial distance. In the next section, we show that this enrichment is also extremely efficient for assemblies of two cylinders. This is an unexpected result, since introduction of a second cylinder in general breaks the axisymmetry that underlies the proposed enrichment [see Eq. (74)].

5. Applications to two-cylinder systems

In this section we consider three configurations of two cylinders. In all three cases, the aspect ratio of the cylinders is $L/R = 50$ and the contrast is $\sigma_1/\sigma_0 = 10^6$. We show that even for cylinders that are very close, interactions are well captured with relatively low polynomial orders (all EIM simulations are performed with $p = 8$ in the present section).

For all configurations, the EIM estimates are compared to FEM reference calculations. Here again, these calculations were done with COMSOL Multiphysics® 5.6. The boundary conditions were replaced with conditions at the boundary of a large sphere (radius: $20L$). The size of the smallest element is $R/3$. The results are plotted in Figs. 9, 10 and 11. We also show the solution for a unique cylinder ("FEM Eshelby"), which allows to quantify the effect of interactions between cylinders.

Two coaxial cylinders. We first consider two coaxial cylinders subjected to an external field $\overline{\mathbf{E}} = \overline{E}\,\mathbf{e}_z$ at infinity, where $\mathbf{e}_z$ denotes the orientation of the cylinders. The gap between the cylinders is $2R$ (center-to-center distance: $2L + 2R$). Results presented in Fig. 9 show an excellent agreement with the reference, FEM solution. Comparison with the "Eshelby FEM" solution shows that the second cylinder increases the electric field within the first cylinder ("positive interactions").

Two parallel cylinders. We now consider two parallel cylinders subjected to an external field $\overline{\mathbf{E}} = \overline{E}\,\mathbf{e}_z$ at infinity, where $\mathbf{e}_z$ corresponds to the orientation of the cylinders. The gap the between cylinders is $2R$ (axis-to-axis distance: $4R$). Again, an excellent agreement is observed (see Fig. 10). Note that in this case, interactions are "negative": the electric field is lower than in the case of an isolated cylinder.

Two coplanar cylinders at 45°. We finally consider two coplanar cylinders, that make a 45° angle (see sketch in Fig. 11, where the distance between the two cylinders is also indicated). The system is subjected to an external field

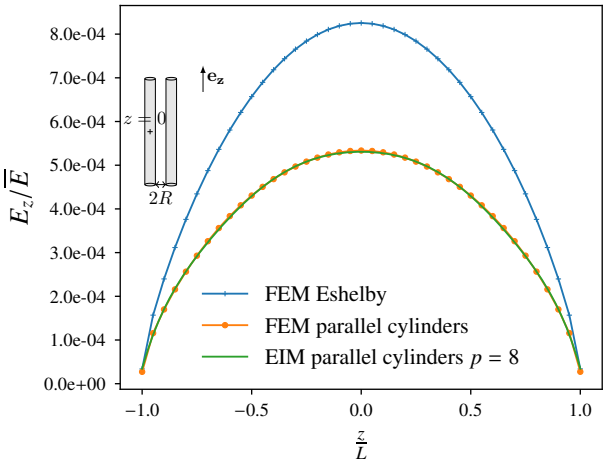

Figure 10: Two parallel cylinders with aspect ratio $L/R = 50$ and contrast $\sigma_1/\sigma_0 = 10^6$, subjected to an external electric field $\overline{\mathbf{E}} = \overline{E}\,\mathbf{e}_z$. The gap between the cylinders is $2R$ (axis-to-axis distance: $4R$). The sectional average of the longitudinal component of the electric field E_z is plotted against the longitudinal coordinate z. "FEM Eshelby": finite element simulation for an isolated cylinder; "FEM parallel cylinders": finite element reference solution; "EIM parallel cylinders $p = 8$": equivalent inclusion method with polynomials of order 8.

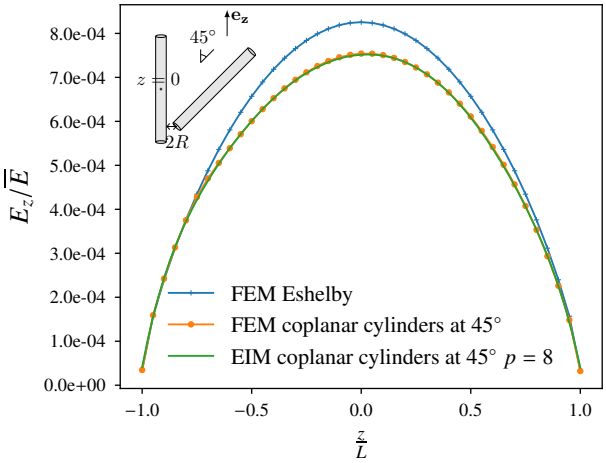

Figure 11: Two coplanar cylinders at 45°, with aspect ratio $L/R = 50$ and contrast $\sigma_1/\sigma_0 = 10^6$, subjected to an external electric field $\overline{\mathbf{E}} = \overline{E}\,\mathbf{e}_z$. The sectional average of the longitudinal component of the electric field E_z is plotted against the longitudinal coordinate z. "FEM Eshelby": finite element simulation for an isolated cylinder; "FEM parallel cylinders": finite element reference solution; "EIM parallel cylinders $p = 8$": equivalent inclusion method with polynomials of order 8.

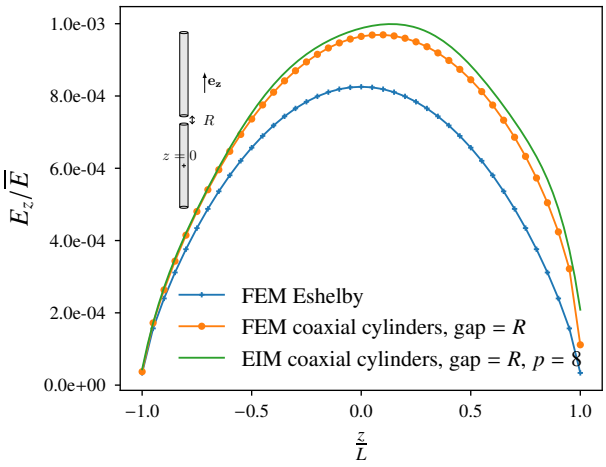

Figure 12: Two coaxial cylinders with aspect ratio $L/R = 50$ and contrast $\sigma_1/\sigma_0 = 10^6$, subjected to an external electric field $\overline{\mathbf{E}} = \overline{E}\,\mathbf{e}_z$. The gap between the cylinders is R (center-to-center distance: $2L + R$). The sectional average of the longitudinal component of the electric field E_z is plotted against the longitudinal coordinate z. FEM Eshelby: finite element simulation for an isolated cylinder; FEM coaxial cylinders: finite element reference solution; EIM coaxial cylinders $p = 8$: equivalent inclusion method with polynomials of order 8. Note that the gap between the cylinders is twice as small as in Fig. 9, which affects negatively the quality of the EIM solution.

$\overline{\mathbf{E}} = \overline{E}\,\mathbf{e}_z$ at infinity, where $\mathbf{e}_z$ corresponds to the orientation of the first cylinder. Although this case breaks many symmetries, the EIM results are just as good as previously (see Fig. 11). Interactions are again "negative".

Contrary to the cases considered in Sec. 4, the three examples presented above involve the interaction coefficients T_{12}^{kl} between the two inclusions of the system. Since our implementation of the method relies on a multipole expansion of these coefficients, it is expected that the accuracy of the EIM decreases for cylinders that get closer. This is not so for cylinders that are separated by a gap $\sim 2R$. Below this limit differences with the FEM reference solution become noticeable. This is illustrated in Fig. 12, where the gap between the two coaxial cylinders is now R.

In the previous section, the EIM was shown to perform remarkably well for a wide range of two-cylinder systems. In the next section, this method is applied to a few larger assemblies. Both the accuracy and efficiency of the method are assessed (in Secs. 6.1 and 6.2, respectively).

6. Application to larger systems

Unless otherwise noted, the EIM is applied in this section with the enrichment introduced in Sec. 4.2 and $p = 8$ (which was shown to deliver excellent results for small assemblies of cylinders).

6.1. Assessment of accuracy

In this first application, we consider two assemblies of 133 cylindrical inhomogeneities, embedded in a spherical domain, the radius of which is adjusted so as to ensure that the total volume fraction of inhomogeneities is 1%. The microstructures are generated by random sequential addition, *making sure that one cylinder is placed vertically at the center of the sphere*. The first of the two microstructures considered here is shown in Fig. 13.

This microstructure is subjected to a macroscopic electric field $\overline{\mathbf{E}} = \overline{E}\,\mathbf{e}_z$ and we compute the longitudinal electric field E_z in the central fiber. Since boundary conditions apply at infinity in the EIM, it was necessary for the FEM simulations to embed the spherical RVE into a larger, homogeneous spherical domain (see Fig. 13). In the present application, the radius of the external sphere is $5\times$ the radius of the spherical RVE. The results are shown for both microstructures in Fig. 14. The agreement is excellent for the first sample, and very satisfactory for the second sample. This confirms that the EIM delivers accurate results, even for complex systems. Note that for the second sample, the longitudinal component of the electric field E_z exhibits a large gradient at $z \simeq -0.7L$. This "near-discontinuity" is

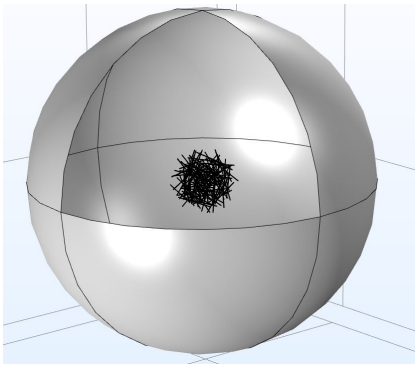

Figure 13: One of the microstructures considered in Sec. 6.1. The total number of cylinders is 133, the volume fraction is 1%. The outer sphere marks the boundary of the FE simulation domain (5× the radius of the RVE).

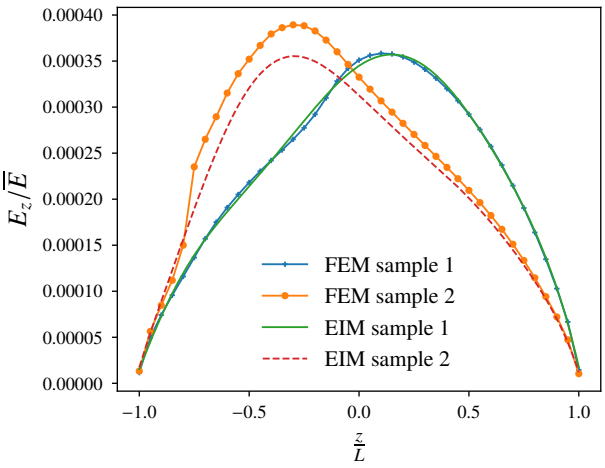

Figure 14: The longitudinal component of the electric field E_z along the central cylindrical inhomogeneity, for the two microstructures considered in Sec. 6.1. "FEM": finite element reference solution; "EIM": equivalent inclusion method with polynomials of order $p = 8$. The agreement is generally very good, slightly better for sample 1.

induced by the presence of another cylinder in the close vicinity of the central cylinder. Of course, polynomials are not well suited to capturing such sharp variations, which explains why the EIM estimate is somewhat less accurate in that case.

Interestingly, we did the same comparison with our initial version of the EIM (no enrichment). The results are displayed in Fig. 15; comparison with Fig. 14 shows that even in highly non-axisymmetric situations, the enrichment introduced in Sec. 4.2 leads to a noticeable improvement of the results.

6.2. *Assessment of efficiency*

Our goal in future work is to compute the effective properties of fibrous materials. In the present section, we discuss wether the EIM can be considered as a convincing competitor to standard finite elements. For the comparison to be as fair as possible, the FEM will be applied in periodic boundary conditions (meshing the external sphere as in the previous application being extremely inefficient). We therefore need to consider *two* microstructures with same number (509) and volume fraction (2%) of cylinders. The first microstructure (FEM) is cubic and periodic (see Fig. 16, left), while the second microstructure (EIM) is spherical (see Fig. 16, right).

Again, both systems are subjected to a macroscopic electric field $\overline{\mathbf{E}} = \overline{E}\,\mathbf{e}_z$. Contrary to the previous section, we do not compare the numerical results *per se* (the microstructures being different, the results will be different!) Rather, we compare both methods in terms of number of unknowns and computation time.

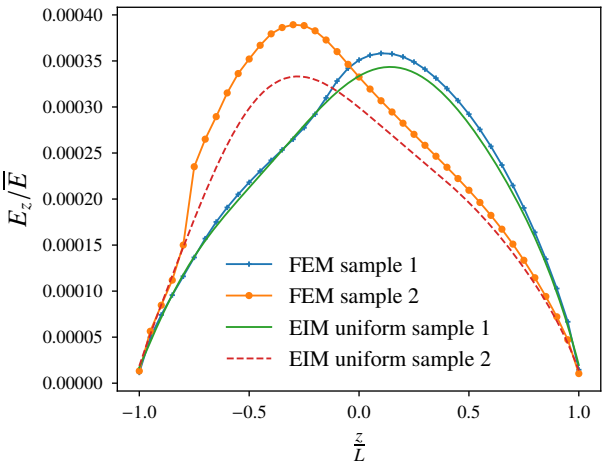

Figure 15: Same as in Fig. 14, without the enrichment introduced in Sec. 4.2.

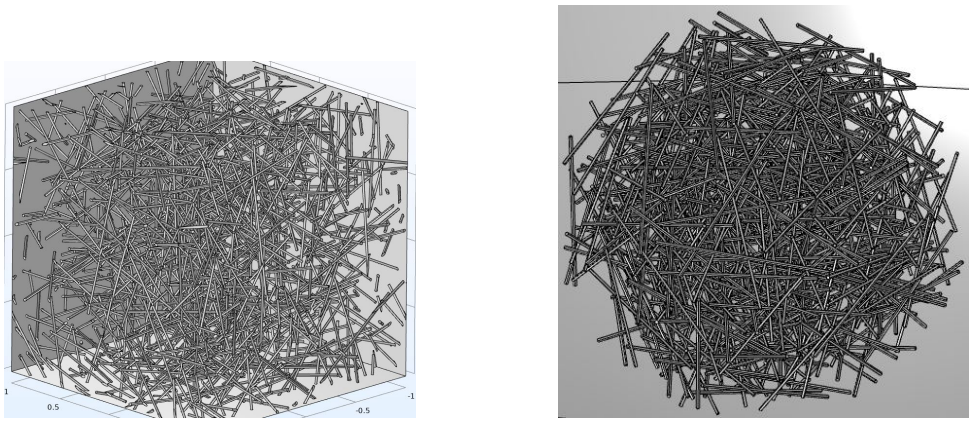

Figure 16: The two microstructures considered in Sec. 6.2. *Left:* a periodic microstructure, to be computed by FEM; *right:* a spherical microstructure, to be computed by EIM. In both microstructures, the total number of cylinders is 509 and the volume fraction is 2 %.

As for the number of unknowns, it amounts to about 15 millions for the FEM, vs. 18324 for the EIM. Clearly, the gain is huge. In terms of computation time, the situation is less clear. Indeed, COMSOL Multiphysics® 5.6 turns out to be only a few times slower than the EIM code. This seemingly disappointing result should be balanced with the observation that our home-made, unoptimized, EIM code is confronted with a commercial, highly optimized FEM code.

Improving the speed of our code is clearly a perspective of the present work. We are confident that we could reach a $10\times$ improvement. Indeed, fine-grained observation of the calculation times in our EIM code shows that the total computation time is largely dominated by the time spent in evaluating the influence tensors. Note that this operation is embarassingly parallel[3] and that appropriate multipolar methods should also help reduce dramatically the total number of influence tensors to be computed.

To close this section, it is observed that the same comparison has been attempted for assemblies of 1018 fibers. In that more challenging case, the FEM simulation *failed*, contrary to the EIM. This again advocates for the latter method.

Remark 5. *In a periodic setting, FFT-based homogenization methods [25, 30] are usually considered as an efficient alternative to finite elements. This is not true of the present case. Indeed, the former requires uniform grids and the cell-size is given by the cross-section of the (slender) cylinders. There is no such requirement for the latter, and the mesh is in fact* refined *in the vicinity of the cylinders (see Fig. 17), which we believe makes the FEM more efficient. A rough estimate of the number of unknowns required for a FFT-based simulation can be obtained as follows. First, the size a of the cubic domain is given by the following expression*

$$\frac{a^3}{R^3} = \frac{2\pi\mathcal{N}}{f}\frac{L}{R},$$

where $\mathcal{N}$ is the total number of cylinders and f the volume fraction. The total number of grid cells is N^3, where $N = a/h$ is the number of subdivisions in each direction (h: cell size). The total number of unknowns is therefore $6N^3$

$$\text{number of dofs (FFT)} = 6N^3 = 6\frac{a^3}{R^3}\left(\frac{R}{h}\right)^3 = \frac{12\pi\mathcal{N}}{f}\frac{L}{R}\left(\frac{R}{h}\right)^3 = \frac{12\pi\times 509\times 50}{0.02}\left(\frac{R}{h}\right)^3 \simeq 48\times 10^6\left(\frac{R}{h}\right)^3$$

A reasonable minimum value of h would be $h = 2R/3$ (3 grid cells for one diameter); then

$$\frac{\text{number of dofs (FFT)}}{\text{number of dofs (FEM)}} \simeq \frac{48\times 10^6\times 1.5^3}{15\times 10^6} \simeq 10.8.$$

7. Conclusion and outlook

In this paper, we have specialized the equivalent inclusion method to slender cylinders. Contrary to the case of spherical inclusions considered by Brisard et al. [7], the proposed method proves extremely efficient in three dimensions. This is due to the fact that the slenderness of the inclusions allowed us to select shape functions that are poorly resolved in the transverse direction, thus avoiding the "curse of dimensionality".

First applications to isolated cylinders indicated a simple enrichment that is then assessed in more complex situations. In all the examples considered in this paper, the estimated fields are very close to the reference FEM calculations. The cost of EIM simulations is however much lower than their FEM counterparts, as the number of degrees of freedom grows linearly with the number of cylinders (rather than linearly with the volume of the simulation domain for FEM). Besides, the EIM remains meaningful for very slender cylinders, a situation where the FEM would struggle, owing to the fineness of the required mesh.

This work opens a series of interesting perspectives. First, we will apply the equivalent inclusion method to large assemblies of cylinders (several thousands of inclusions) in order to estimate homogenized conductivities of fibrous media. In order to benefit from the full potential of the EIM, we will however need to optimize the assembly phase.

[3] https://en.wikipedia.org/wiki/Embarrassingly_parallel, last retrieved 2023-01-11.

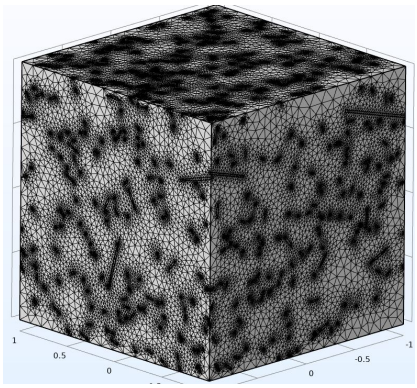

Figure 17: Mesh of one of the microstructures considered in Sec 6.2 for the finite element simulations. Note that the mesh is refined in the vicinity of the cylinders, which would not have been possible with e.g. FFT-based methods (see also remark 5).

It has been observed in this paper that enriching the trial polarization with a radial component, linear in the radial distance, delivers suprisingly good results. A second perspective is therefore investigating why this is so and what the "optimal" enrichment is. We expect the method to apply to all physical problems where a Green operator can be defined. We will consider the natural extension to linear elasticity as another perspective. Finally, the interaction coefficients are approximated to first order in the present work. This probably leads to increased errors for densely packed assemblies. Higher-order estimates of the interaction coefficients will also be investigated.

CRediT authorship contribution statement

Antoine Martin: Conceptualization, Methodology, Software, Validation, Formal Analysis, Investigation, Writing - Original Draft, Visualization — **Sébastien Brisard:** Conceptualization, Resources, Writing - Review & Editing, Supervision, Project Administration — **Stéphane Deleville:** Writing - Review & Editing, Supervision, Project administration — **Karam Sab:** Conceptualization, Resources, Writing - Review & Editing, Funding Acquisition

A. On the Green operator

In this appendix, we provide a formal definition of the Green operator $\mathbf{\Gamma}_0^\infty$ introduced in the main text. This operator is defined from the solution to the following problem [18, 40, 19] posed over the whole space $\mathbb{R}^3$

$$\operatorname{div} \mathbf{j} = 0, \tag{A.1}$$

$$\mathbf{j} = \boldsymbol{\sigma}_0 \cdot \mathbf{E} + \boldsymbol{\tau}, \tag{A.2}$$

$$\mathbf{E} = \mathbf{grad}\, \phi, \tag{A.3}$$

with the requirement that $\mathbf{E}$ be square integrable over $\mathbb{R}^3$. In the above problem, $\boldsymbol{\tau}$ is a prescribed square integrable vector field. This problem is well-posed [8]. Owing to linearity, its unique solution depends linearly on the sole loading parameter, namely: the field $\boldsymbol{\tau}$. In particular, the polarization field $\boldsymbol{\tau}$ is mapped linearly onto the electric field $\mathbf{E}$. The linear mapping $\boldsymbol{\tau} \mapsto -\mathbf{E}$ (note the minus sign) will be called Green operator. In other words, $[-\mathbf{\Gamma}_0^\infty(\boldsymbol{\tau})]$ is the electric field induced over $\mathbb{R}^3$ by the polarization $\boldsymbol{\tau}$

B. Derivation of the linear system of the EIM

To derive the system (26), expressions (23) and (25) are substituted into the discrete variational problem (17). We find first, using the general identity (20) (with $\boldsymbol{\varpi} = \mathbf{0}$ in Ω_0)

$$\langle \boldsymbol{\varpi}^p \rangle = \sum_\alpha f_\alpha \langle \boldsymbol{\varpi}^p \rangle_\alpha = \sum_{\alpha,k} f_\alpha \langle \mathbf{\Psi}_\alpha^k \varpi_\alpha^k \rangle_\alpha = \sum_{\alpha,k} f_\alpha \varpi_\alpha^k \mathbf{M}_\alpha^k, \tag{B.1}$$

where $\mathbf{M}_\alpha^k$ is defined by Eq. (29). We now turn to the first term of the bilinear form a [see Eq. (16)] and use again identity (20)

$$\begin{aligned}\langle \boldsymbol{\varpi}^p \cdot (\boldsymbol{\sigma} - \boldsymbol{\sigma}_0)^{-1} \cdot \boldsymbol{\tau}^p \rangle &= \sum_\alpha f_\alpha \langle \boldsymbol{\varpi}^p \cdot (\boldsymbol{\sigma} - \boldsymbol{\sigma}_0)^{-1} \cdot \boldsymbol{\tau}^p \rangle_\alpha = \sum_{\alpha,k,l} f_\alpha \langle \varpi_\alpha^k \boldsymbol{\Psi}_\alpha^k \cdot (\boldsymbol{\sigma}_\alpha - \boldsymbol{\sigma}_0)^{-1} \cdot \boldsymbol{\Psi}_\alpha^l \tau_\alpha^l \rangle_\alpha \\ &= \sum_{\alpha,k,l} f_\alpha \varpi_\alpha^k \langle \boldsymbol{\Psi}_\alpha^k \cdot (\boldsymbol{\sigma}_\alpha - \boldsymbol{\sigma}_0)^{-1} \cdot \boldsymbol{\Psi}_\alpha^l \rangle_\alpha \tau_\alpha^l = \sum_{\alpha,k,l} f_\alpha \varpi_\alpha^k R_\alpha^{kl} \tau_\alpha^l, \end{aligned} \tag{B.2}$$

where we used in the second line that over Ω_α, $\boldsymbol{\sigma} = \boldsymbol{\sigma}_\alpha$, $\boldsymbol{\tau}^p = \sum_l \boldsymbol{\Psi}_\alpha^l \tau_\alpha^l$ and $\boldsymbol{\varpi}^p = \sum_k \boldsymbol{\Psi}_\alpha^k \varpi_\alpha^k$.

Finally, owing to the linearity of the $\boldsymbol{\Gamma}_0^\infty$ operator, the last term of the bilinear form a [see Eq. (16)] reads

$$\begin{aligned}\langle \boldsymbol{\varpi} \cdot \boldsymbol{\Gamma}_0^\infty(\boldsymbol{\tau} - \chi\langle\boldsymbol{\tau}\rangle)\rangle &= \langle \boldsymbol{\varpi} \cdot \boldsymbol{\Gamma}_0^\infty(\boldsymbol{\tau})\rangle - \langle \boldsymbol{\varpi} \cdot \boldsymbol{\Gamma}_0^\infty(\chi\langle\boldsymbol{\tau}\rangle)\rangle = \langle \boldsymbol{\varpi} \cdot \boldsymbol{\Gamma}_0^\infty(\boldsymbol{\tau})\rangle - \langle \boldsymbol{\varpi} \cdot \mathbf{P}_0 \cdot \langle\boldsymbol{\tau}\rangle\rangle \\ &= \langle \boldsymbol{\varpi} \cdot \boldsymbol{\Gamma}_0^\infty(\boldsymbol{\tau})\rangle - \langle \boldsymbol{\varpi}\rangle \cdot \mathbf{P}_0 \cdot \langle\boldsymbol{\tau}\rangle = \langle \boldsymbol{\varpi} \cdot \boldsymbol{\Gamma}_0^\infty(\boldsymbol{\tau})\rangle - \sum_{\alpha,\beta,k,l} f_\alpha f_\beta \varpi_\alpha^k \mathbf{M}_\alpha^k \cdot \mathbf{P}_0 \cdot \mathbf{M}_\beta^l \tau_\beta^l, \end{aligned} \tag{B.3}$$

where the second line results from the application of the results of Eshelby [11] to the spherical domain Ω and the constant polarization $\langle\boldsymbol{\tau}\rangle$. The first term of Eq. (B.3) is then expanded with identity (20)

$$\langle \boldsymbol{\varpi} \cdot \boldsymbol{\Gamma}_0^\infty(\boldsymbol{\tau})\rangle = \sum_{\alpha,k} f_\alpha \langle \varpi_\alpha^k \boldsymbol{\Psi}_\alpha^k \cdot \boldsymbol{\Gamma}_0^\infty(\boldsymbol{\tau})\rangle_\alpha = \sum_{\alpha,\beta,k,l} f_\alpha \varpi_\alpha^k \langle \boldsymbol{\Psi}_\alpha^k \cdot \boldsymbol{\Gamma}_0^\infty(\boldsymbol{\Psi}_\beta^l \tau_\beta^l)\rangle_\alpha = \sum_{\alpha,\beta,k,l} f_\alpha \varpi_\alpha^k T_{\alpha\beta}^{kl} \tau_\beta^l, \tag{B.4}$$

where the coefficients $T_{\alpha\beta}^{kl}$ are defined by Eq. (28). Gathering Eqs. (B.1), (B.2) and (B.4) delivers the following variational problem: find $\tau_\alpha^k \in \mathbb{R}$ ($\alpha = 1, \ldots, N$ and $k = 0, \ldots, K_p - 1$) such that, for all $\varpi_\beta^l \in \mathbb{R}$ ($\beta = 1, \ldots, N$ and $l = 0, \ldots, K_p - 1$)

$$\sum_{\alpha,k} f_\alpha \varpi_\alpha^k R_\alpha^{kl} \tau_\alpha^l + \sum_{\alpha,\beta,k,l} f_\alpha \varpi_\alpha^k T_{\alpha\beta}^{kl} \tau_\beta^l - \sum_{\alpha,\beta,k,l} f_\alpha f_\beta \varpi_\alpha^k \mathbf{M}_\alpha^k \cdot \mathbf{P}_0 \cdot \mathbf{M}_\beta^l \tau_\beta^l = \sum_{\alpha,k} f_\alpha \varpi_\alpha^k \mathbf{M}_\alpha^k \cdot \overline{\mathbf{E}}, \tag{B.5}$$

In turn, the above variational problem reduces to the linear system (26).

C. Retrieving the self-influence coefficient from the elementary potentials Φ_1 and Φ_3

Eqs. (65) and (66) show that the electric potential ϕ can be reconstructed from the elementary potentials Φ_1 and Φ_3

$$\phi(r, \theta, z) = \left[\Phi_1(r, z)\mathbf{e}_r + \Phi_3(r, z)\,\mathbf{e}_z\right] \cdot \mathbf{e}_j, \tag{C.1}$$

and, taking the gradient

$$\mathbf{E} = \frac{\partial \phi}{\partial r}\mathbf{e}_r + \frac{1}{r}\frac{\partial \phi}{\partial \theta}\mathbf{e}_\theta + \frac{\partial \phi}{\partial z}\mathbf{e}_z = \left(\frac{\partial \Phi_1}{\partial r}\mathbf{e}_r \otimes \mathbf{e}_r + \frac{\partial \Phi_3}{\partial r}\mathbf{e}_r \otimes \mathbf{e}_z + \frac{\Phi_1}{r}\mathbf{e}_\theta \otimes \mathbf{e}_\theta + \frac{\partial \Phi_1}{\partial z}\mathbf{e}_z \otimes \mathbf{e}_r + \frac{\partial \Phi_3}{\partial z}\mathbf{e}_z \otimes \mathbf{e}_z\right) \cdot \mathbf{e}_j. \tag{C.2}$$

S_α^{mn} is retrieved from the volume average (weighted by $\psi_\alpha^m \mathbf{e}_i$) over the cylindrical inclusion Ω_α of the above quantity

$$(\mathsf{S}_\alpha^{mn})_{ij} = -\frac{1}{2\pi R^2 L}\int_{-L}^{+L}\int_0^{2\pi}\int_0^R r\,\psi_\alpha^m \mathbf{e}_i \cdot \left(\frac{\partial \Phi_1}{\partial r}\mathbf{e}_r \otimes \mathbf{e}_r + \frac{\partial \Phi_3}{\partial r}\mathbf{e}_r \otimes \mathbf{e}_z + \frac{\Phi_1}{r}\mathbf{e}_\theta \otimes \mathbf{e}_\theta + \frac{\partial \Phi_1}{\partial z}\mathbf{e}_z \otimes \mathbf{e}_r + \frac{\partial \Phi_3}{\partial z}\mathbf{e}_z \otimes \mathbf{e}_z\right) \cdot \mathbf{e}_j \,\mathrm{d}r\,\mathrm{d}\theta\,\mathrm{d}z. \tag{C.3}$$

Upon integration with respect to θ, observing that the following identities hold (with $\mathbf{e}_z = \mathbf{n}_\alpha$), Eqs. (69) and (70) and are finally retrieved

$$\int_0^{2\pi} \mathbf{e}_r \otimes \mathbf{e}_r \,\mathrm{d}\theta = \int_0^{2\pi} \mathbf{e}_\theta \otimes \mathbf{e}_\theta \,\mathrm{d}\theta = \pi(\mathbf{g}_1 \otimes \mathbf{g}_1 + \mathbf{g}_2 \otimes \mathbf{g}_2) = \pi(\mathbf{1} - \mathbf{e}_z \otimes \mathbf{e}_z), \tag{C.4}$$

$$\int_0^{2\pi} \mathbf{e}_r \otimes \mathbf{e}_z \,\mathrm{d}\theta = \int_0^{2\pi} \mathbf{e}_z \otimes \mathbf{e}_r \,\mathrm{d}\theta = 0. \tag{C.5}$$

D. Retrieving S_α^{mn} and $\mathsf{T}_{\alpha\beta}^{mn}$ with the enriched discretization

D.1. Determination of $\mathsf{T}_{\alpha\beta}^{mn}$

We first notice that $\left(\mathsf{T}_{\alpha\beta}^{mn}\right)_{ij}$ has already been computed for $i,j=1,2,3$. We then have to compute $\left(\mathsf{T}_{\alpha\beta}^{mn}\right)_{ij}$ when $i=4$ or $j=4$. Let us begin with $i=4$ and $j=1,2,3$. Eq (48) must be replaced by

$$\mathsf{T}_{\alpha\beta}^{mn} = \sigma_0^{-1}\left(\mathsf{U}_{\alpha\beta}^{mn} - \mathsf{V}_{\alpha\beta}^{mn}\right) \tag{D.1}$$

where $\mathsf{U}_{\alpha\beta}^{mn}$ is a 4×4 matrix and

$$\left(\mathsf{U}_{\alpha\beta}^{mn}\right)_{4j} = \frac{1}{4\pi\, V_\alpha}\int_{\mathbf{y}_\alpha\in\Omega_\alpha}\int_{\mathbf{y}_\beta\in\Omega_\beta}\frac{z_\alpha^m\, z_\beta^n}{\|\mathbf{y}_\beta-\mathbf{y}_\alpha\|^3}\, r_\alpha \mathbf{e}_{r,\alpha}\cdot\mathbf{e}_j\, \mathrm{d}^3\mathbf{y}_\beta\, \mathrm{d}^3\mathbf{y}_\alpha, \tag{D.2}$$

and

$$\left(\mathsf{V}_{\alpha\beta}^{mn}\right)_{4j} = \frac{3}{4\pi\, V_\alpha}\int_{\mathbf{y}_\alpha\in\Omega_\alpha}\int_{\mathbf{y}_\beta\in\Omega_\beta} z_\alpha^m\, z_\beta^n\, r_\alpha \frac{\mathbf{e}_{r,\alpha}\cdot(\mathbf{y}_\beta-\mathbf{y}_\alpha)}{\|\mathbf{y}_\beta-\mathbf{y}_\alpha\|^5}(\mathbf{y}_\beta-\mathbf{y}_\alpha)_j\, \mathrm{d}^3\mathbf{y}_\beta\, \mathrm{d}^3\mathbf{y}_\alpha, \tag{D.3}$$

for $i,j=1,2,3$. We perform the same multipole expansion as in Section 3.2, when R is small compared to the smallest inter-fiber distance. Eqs (59) and (60) then have to be replaced by

$$\left(\mathsf{U}_{\alpha\beta}^{mn}\right)_{4j} = \frac{L^{m+n+3}}{8\pi^2}\frac{R^3}{L^2}\int \frac{\rho_\alpha^2\,\rho_\beta\,\zeta_\alpha^m\,\zeta_\beta^n}{\|\mathbf{w}^0\|^3}\mathbf{e}_{r,\alpha}\cdot\mathbf{e}_j\, \mathrm{d}\zeta_\alpha\, \mathrm{d}\zeta_\beta\, \mathrm{d}\theta_\alpha\, \mathrm{d}\theta_\beta\, \mathrm{d}\rho_\alpha\, \mathrm{d}\rho_\beta, \tag{D.4}$$

$$\left(\mathsf{V}_{\alpha\beta}^{mn}\right)_{4j} = \frac{3L^{m+n+3}}{8\pi^2}\frac{R^3}{L^2}\int \frac{\rho_\alpha^2\,\rho_\beta\,\zeta_\alpha^m\,\zeta_\beta^n}{\|\mathbf{w}^0\|^5}(\mathbf{e}_{r,\alpha}\cdot\mathbf{w}^0)w_j^0\, \mathrm{d}\zeta_\alpha\, \mathrm{d}\zeta_\beta\, \mathrm{d}\theta_\alpha\, \mathrm{d}\theta_\beta\, \mathrm{d}\rho_\alpha\, \mathrm{d}\rho_\beta. \tag{D.5}$$

Because of the integration on cylinder α upon θ_α, the two terms are null. It is the same when $j=4$ because of the integration upon θ_β. Then, when $i=4$ or $j=4$, $\left(\mathsf{T}_{\alpha\beta}^{mn}\right)_{ij}$ is null.

D.2. Determination of S_α^{mn}

As for $\mathsf{T}_{\alpha\beta}^{mn}$, $(\mathsf{S}_\alpha^{mn})_{ij}$ has already been computed for $i,j=1,2,3$. We then have to consider the cases $i=4$ or $j=4$. Let us begin with $i=4$ and $j=1,2,3$. Here Eqs (C.1) and (C.2) are still valid, but Eq (C.3) must be replaced with

$$(\mathsf{S}_\alpha^{mn})_{4j} = -\frac{1}{2\pi R^2 L}\int_{-L}^{+L}\int_0^{2\pi}\int_0^R r^2\,\psi_\alpha^m \mathbf{e}_r\cdot\left(\frac{\partial\Phi_1}{\partial r}\mathbf{e}_r\otimes\mathbf{e}_r+\frac{\partial\Phi_3}{\partial r}\mathbf{e}_r\otimes\mathbf{e}_z+\frac{\Phi_1}{r}\mathbf{e}_\theta\otimes\mathbf{e}_\theta+\frac{\partial\Phi_1}{\partial z}\mathbf{e}_z\otimes\mathbf{e}_r+\frac{\partial\Phi_3}{\partial z}\mathbf{e}_z\otimes\mathbf{e}_z\right)\cdot\mathbf{e}_j\, \mathrm{d}r\, \mathrm{d}\theta\, \mathrm{d}z. \tag{D.6}$$

and then

$$(\mathsf{S}_\alpha^{mn})_{4j} = -\frac{1}{2\pi R^2 L}\int_{-L}^{+L}\int_0^{2\pi}\int_0^R r^2\,\psi_\alpha^m\left(\frac{\partial\Phi_1}{\partial r}\mathbf{e}_r+\frac{\partial\Phi_3}{\partial r}\mathbf{e}_z\right)\cdot\mathbf{e}_j\, \mathrm{d}r\, \mathrm{d}\theta\, \mathrm{d}z. \tag{D.7}$$

Let us now consider the case $j=4$. The polarization is now $\psi_\alpha^n r\,\mathbf{e}_r$. It is axisymmetric. Then Eq (66) must be replaced with $\phi(r,\theta,z)=\Phi_4(r,z)$, where Φ_4 solves the following variational problem

$$\sigma_0\int_{-\infty}^{+\infty}\int_0^{+\infty} r\left(\frac{\partial\Phi_4}{\partial r}\frac{\partial\hat{\Phi}}{\partial r}+\frac{\partial\Phi_4}{\partial z}\frac{\partial\hat{\Phi}}{\partial z}\right)\mathrm{d}r\, \mathrm{d}z+\int_{-L}^{+L}\int_0^R r^2\,\psi_\alpha^n(z)\frac{\partial\hat{\Phi}}{\partial r}\, \mathrm{d}r\, \mathrm{d}z = 0. \tag{D.8}$$

We then take the gradient of Φ_4

$$\mathbf{E} = \frac{\partial\Phi_4}{\partial r}\mathbf{e}_r+\frac{\partial\Phi_4}{\partial z}\mathbf{e}_z \tag{D.9}$$

and when $i=1,2,3$,

$$(\mathsf{S}_\alpha^{mn})_{i4} = -\frac{1}{2\pi R^2 L}\int_{-L}^{+L}\int_0^{2\pi}\int_0^R r\,\psi_\alpha^m\frac{\partial\Phi_4}{\partial z}\mathbf{e}_i\cdot\mathbf{e}_z\, \mathrm{d}r\, \mathrm{d}\theta\, \mathrm{d}z. \tag{D.10}$$

whereas when $i=4$:

$$(\mathsf{S}_\alpha^{mn})_{44} = -\frac{1}{2\pi R^2 L}\int_{-L}^{+L}\int_0^{2\pi}\int_0^R r^2\,\psi_\alpha^m\frac{\partial\Phi_4}{\partial r}\, \mathrm{d}r\, \mathrm{d}\theta\, \mathrm{d}z. \tag{D.11}$$

References

[1] Adessina, A., Barthélémy, J.F., Ben Fraj, A., 2020. Micromechanical model for the diffusion properties of materials embedding complex structures. Mechanics of Materials 146, 103404. doi:10.1016/j.mechmat.2020.103404.

[2] Adessina, A., Barthélémy, J.F., Lavergne, F., Ben Fraj, A., 2017. Effective elastic properties of materials with inclusions of complex structure. International Journal of Engineering Science 119, 1–15. doi:10.1016/j.ijengsci.2017.03.015.

[3] Alnæs, M., Blechta, J., Hake, J., Johansson, A., Kehlet, B., Logg, A., Richardson, C., Ring, J., Rognes, M.E., Wells, G.N., 2015. The FEniCS Project Version 1.5. Archive of Numerical Software 3. doi:10.11588/ans.2015.100.20553.

[4] Benedikt, B., Lewis, M., Rangaswamy, P., 2006. On elastic interactions between spherical inclusions by the equivalent inclusion method. Computational Materials Science 37, 380–392. doi:10.1016/j.commatsci.2005.10.002.

[5] Biercuk, M.J., Llaguno, M.C., Radosavljevic, M., Hyun, J.K., Johnson, A.T., Fischer, J.E., 2002. Carbon nanotube composites for thermal management. Applied Physics Letters 80, 2767–2769. doi:10.1063/1.1469696.

[6] Brandt, A.M., 2008. Fibre reinforced cement-based (FRC) composites after over 40 years of development in building and civil engineering. Composite Structures 86, 3–9. doi:10.1016/j.compstruct.2008.03.006.

[7] Brisard, S., Dormieux, L., Sab, K., 2014. A variational form of the equivalent inclusion method for numerical homogenization. International Journal of Solids and Structures 51, 716–728. doi:10.1016/j.ijsolstr.2013.10.037.

[8] Brisard, S., Sab, K., Dormieux, L., 2013. New boundary conditions for the computation of the apparent stiffness of statistical volume elements. Journal of the Mechanics and Physics of Solids 61, 2638–2658. doi:10.1016/j.jmps.2013.08.009.

[9] Brown, W.F., 1955. Solid Mixture Permittivities. The Journal of Chemical Physics 23, 1514–1517. doi:doi:10.1063/1.1742339.

[10] El Mouden, M., Molinari, A., 2000. Thermoelastic Properties of Composites Containing Ellipsoidal Inhomogeneities. Journal of Thermal Stresses 23, 233–255. doi:10.1080/014957300280425.

[11] Eshelby, J.D., 1957. The Determination of the Elastic Field of an Ellipsoidal Inclusion, and Related Problems. Proceedings of the Royal Society of London. Series A, Mathematical and Physical Sciences 241, 376–396. doi:10.1098/rspa.1957.0133.

[12] Fond, C., Géhant, S., Schirrer, R., 2002. Effects of mechanical interactions on the hydrostatic stress in randomly distributed rubber particles in an amorphous polymer matrix. Polymer 43, 909–919. doi:10.1016/S0032-3861(01)00621-8.

[13] Hiroshi, H., Minoru, T., 1986. Equivalent inclusion method for steady state heat conduction in composites. International Journal of Engineering Science 24, 1159–1172. doi:10.1016/0020-7225(86)90011-X.

[14] Hori, M., Nemat-Nasser, S., 1993. Double-inclusion model and overall moduli of multi-phase composites. Mechanics of Materials 14, 189–206. doi:10.1016/0167-6636(93)90066-Z.

[15] Kabel, M., Merkert, D., Schneider, M., 2015. Use of composite voxels in FFT-based homogenization. Computer Methods in Applied Mechanics and Engineering 294, 168–188. doi:10.1016/j.cma.2015.06.003.

[16] Kanit, T., Forest, S., Galliet, I., Mounoury, V., Jeulin, D., 2003. Determination of the size of the representative volume element for random composites: Statistical and numerical approach. International Journal of Solids and Structures 40, 3647–3679. doi:10.1016/S0020-7683(03)00143-4.

[17] Kong, L.B., Li, Z.W., Liu, L., Huang, R., Abshinova, M., Yang, Z.H., Tang, C.B., Tan, P.K., Deng, C.R., Matitsine, S., 2013. Recent progress in some composite materials and structures for specific electromagnetic applications. International Materials Reviews 58, 203–259. doi:10.1179/1743280412Y.0000000011.

[18] Korringa, J., 1973. Theory of elastic constants of heterogeneous media. Journal of Mathematical Physics 14, 509–513. doi:doi:10.1063/1.1666346.

[19] Kröner, E., 1974. On the Physics and Mathematics of Self-Stresses, in: Zeman, J.L., Ziegler, F. (Eds.), Topics in Applied Continuum Mechanics, Springer Verlag Wien, Vienna. pp. 22–38.

[20] Logg, A., Mardal, K.A., Wells, G.N., 2012. Automated Solution of Differential Equations by the Finite Element Method The FEniCS Book. Number 84 in Lecture Notes in Computational Science and Engineering, Springer.

[21] Martin, A., 2022. Computation of Interaction Coefficients of Cylindrical Inhomogeneities. Technical Report. Laboratoire Navier UMR 8205.

[22] Molinari, A., El Mouden, M., 1996. The problem of elastic inclusions at finite concentration. International Journal of Solids and Structures 33, 3131–3150. doi:10.1016/0020-7683(95)00275-8.

[23] Mori, T., Tanaka, K., 1973. Average stress in matrix and average elastic energy of materials with misfitting inclusions. Acta Metallurgica 21, 571–574. doi:10.1016/0001-6160(73)90064-3.

[24] Moschovidis, Z.A., Mura, T., 1975. Two-Ellipsoidal Inhomogeneities by the Equivalent Inclusion Method. Journal of Applied Mechanics 42, 847–852. doi:10.1115/1.3423718.

[25] Moulinec, H., Suquet, P., 1998. A numerical method for computing the overall response of nonlinear composites with complex microstructure. Computer Methods in Applied Mechanics and Engineering 157, 69–94. doi:10.1016/S0045-7825(97)00218-1.

[26] Norris, A., 1985. A differential scheme for the effective moduli of composites. Mechanics of Materials 4, 1–16. doi:10.1016/0167-6636(85)90002-X.

[27] Percy, J.H., Pian, T.H.H., Klein, S., Navaratna, D.R., 1965. Application of matrix displacement method to linear elastic analysis of shells of revolution. AIAA Journal 3, 2138–2145. doi:10.2514/3.3326.

[28] Rodin, G.J., Hwang, Y.L., 1991. On the problem of linear elasticity for an infinite region containing a finite number of non-intersecting spherical inhomogeneities. International Journal of Solids and Structures 27, 145–159. doi:10.1016/0020-7683(91)90225-5.

[29] Sab, K., 1992. On the homogenization and the simulation of random materials. European Journal of Mechanics - A/Solids 11, 585–607.

[30] Schneider, M., 2021. A review of nonlinear FFT-based computational homogenization methods. Acta Mechanica 232, 2051–2100. doi:10.1007/s00707-021-02962-1.

[31] Torquato, S., 1985. Effective electrical conductivity of two-phase disordered composite media. Journal of Applied Physics 58, 3790–3797. doi:10.1063/1.335593.

[32] Vieville, P., Bonnet, A.S., Lipiński, P., 2006. Modelling effective properties of composite materials using the inclusion concept. General considerations. Archives of Mechanics 58, 207–239. doi:10.24423/aom.209.

[33] Walpole, L.J., 1969. On the overall elastic moduli of composite materials. Journal of the Mechanics and Physics of Solids 17, 235–251. doi:10.1016/0022-5096(69)90014-3.
[34] Willis, J., 1977. Bounds and self-consistent estimates for the overall properties of anisotropic composites. Journal of the Mechanics and Physics of Solids 25, 185–202. doi:10.1016/0022-5096(77)90022-9.
[35] Wilson, E.L., 1965. Structural analysis of axisymmetric solids. AIAA Journal 3, 2269–2274. doi:10.2514/3.3356.
[36] Wu, C., Yin, H., 2021. The inclusion-based boundary element method (iBEM) for virtual experiments of elastic composites. Engineering Analysis with Boundary Elements 124, 245–258. doi:10.1016/j.enganabound.2020.12.020.
[37] Yin, H.M., Lee, P.H., Liu, Y.J., 2014. Equivalent Inclusion Method for the Stokes Flow of Drops Moving in a Viscous Fluid. Journal of Applied Mechanics 81. doi:10.1115/1.4027312.
[38] Yu, X.w., Wang, Z.w., Wang, H., 2021. Multiple ellipsoidal/elliptical inhomogeneities embedded in infinite matrix by equivalent inhomogeneous inclusion method. Mathematics and Mechanics of Solids 26, 1798–1814. doi:10.1177/10812865211007194.
[39] Zaoui, A., 2002. Continuum Micromechanics: Survey. Journal of Engineering Mechanics 128, 808–816. doi:10.1061/(ASCE)0733-9399(2002)128:8(808).
[40] Zeller, R., Dederichs, P.H., 1973. Elastic Constants of Polycrystals. Physica Status Solidi (B) 55, 831–842. doi:10.1002/pssb.2220550241.